

# SEEDING CORES: A PATHWAY FOR NUCLEAR STAR CLUSTERS FROM BOUND STAR CLUSTERS IN THE FIRST BILLION YEARS

FRED ANGELO BATAN GARCIA<sup>1,\*</sup>, MASSIMO RICOTTI<sup>2,†</sup>, AND KAZUYUKI SUGIMURA<sup>3</sup>

<sup>1</sup> Department of Astronomy, Columbia University, 538 W 120th Street, New York, NY 10027, USA

<sup>2</sup> Department of Astronomy, University of Maryland, College Park, MD 20742, USA

<sup>3</sup> Faculty of Science, Hokkaido University, Sapporo, Hokkaido 060-0810, Japan

Version March 13, 2025

## Abstract

We model the formation of star clusters in a dwarf galaxy progenitor during the first 700 Myr of cosmic history using a cosmological radiation-hydrodynamic simulation with a realistic sub-grid star formation efficiency (SFE) model, derived from AU-scale radiation-MHD simulations of molecular clouds with varying mass, density, and metallicity. Using this model for cloud-scale SFEs, the galaxy forms stars stochastically, assembling most of its  $10^6 M_{\odot}$  in stars by redshift  $z = 8$  through two star-forming bursts (SFBs), each lasting  $\sim 10$  Myr, separated by 80 Myr of quiescence. Clouds reach SFEs up to 80% during the first SFB, forming bound star clusters (densities  $\sim 10^{2-4} M_{\odot} \text{ pc}^{-2}$ , radii  $\lesssim 3$  pc) resembling those observed by the James Webb Space Telescope (JWST) in strongly lensed galaxies. Star clusters follow a flat power-law mass function with slope  $\Gamma \sim -0.4$ . The most massive star clusters ( $10^{4-5} M_{\odot}$ ) grow through mergers and have metallicity spreads of  $0.05 - 0.1$  dex that roughly scale with mass. The second SFB forms loosely bound star clusters with higher metallicities:  $-1.95 < \log(Z/Z_{\odot}) < -1.50$  at lower SFEs (2 - 20%). At  $z \sim 8.7$ , a nuclear star cluster (NSC) is seeded, growing 83% of its mass ( $2.4 \times 10^5 M_{\odot}$ , 20% of the galaxy's stellar mass) through mergers with pre-existing clusters and the rest through in-situ star formation. The early formation of NSCs has interesting implications for seeding supermassive black holes and the population of *little red dots* recently discovered by JWST at  $z \gtrsim 5$ .

*Subject headings:* galaxies: high-redshift – galaxies: formation – galaxies: star clusters

Stars in our Galaxy form in star clusters which can either be gravitationally bound (e.g., globular clusters) or unbound (e.g., open clusters). This likely holds at high redshifts during the formation of Population III (Pop III) stars in primordial halos ( $z \gtrsim 12$ ) (Bromm & Yoshida 2011) and subsequent Population II (Pop II) stars in early galaxies ( $z \gtrsim 6$ ) (Adamo et al. 2020; Klessen & Glover 2023). The recent launch of the JWST (Gardner et al. 2023) has made — and continues to make — progress in studying this high- $z$  frontier (e.g., Finkelstein et al. 2023; Kokorev et al. 2024a); particularly, in the detection of compact star clusters (tens of parsecs to parsec in size) at  $z \sim 6 - 10$  using gravitational lensing. These bound systems are candidate predecessors of today's globular clusters (GCs) (Vanzella et al. 2023; Adamo et al. 2024b; Mowla et al. 2024; Fujimoto et al. 2024) and therefore continually shape our understanding of star formation in the early Universe.

Detailed numerical studies of star formation in massive ( $\gtrsim 10^5 M_{\odot}$ ) giant molecular clouds (GMCs) link high SFEs to regions of high surface density and pressure (e.g., He et al. 2019; Fukushima & Yajima 2021; Polak et al. 2024; Menon et al. 2024). These conditions are more prevalent at high redshifts, where massive star clusters that likely evolve into GCs today are formed (Shapiro et al. 2010; Kruijssen 2015; Boylan-Kolchin 2024). Recent efforts focus on modelling their formation within a fully cosmological framework in the first galaxies (e.g., Garcia et al. 2023; Rodriguez et al. 2023; Chen & Gnedin 2023; van Donkelaar et al. 2023;

Pfeffer et al. 2024; Calura et al. 2024), with some focused on their roles as drivers of cosmic reionization (Ricotti 2002; Katz & Ricotti 2013; Renzini 2017; Ma et al. 2021).

Star cluster formation may also play a key role in the seeding and growth of supermassive black holes (SMBHs). JWST observations reveal the prevalence of compact ( $\lesssim 200$  pc) high-redshift ( $z \gtrsim 5$ ) objects with red continua, known as little red dots (LRDs) (Akins et al. 2023; Matthee et al. 2024; Greene et al. 2024). Some exhibit line broadening (in some cases as high as FWHM  $\sim 2000 \text{ km s}^{-1}$ ), suggesting masses of  $10^{7-8} M_{\odot}$  (Matthee et al. 2024). Whether these systems are powered by SMBHs or star formation remains uncertain (e.g., Baggen et al. 2024), highlighting the need to understand possible pathways for SMBH seeding.

Several mechanisms have been proposed to explain the rapid early growth of SMBHs, requiring either massive seeds, super-Eddington accretion, or both (see review by Inayoshi et al. 2020). One commonly invoked scenario is the direct collapse black hole scenario where a metal-free, warm ( $10^4$  K) primordial gas cloud avoids fragmentation and collapses into a  $\sim 10^{5-6} M_{\odot}$  seed (e.g., Oh & Haiman 2002; Wise et al. 2019). However, these classes of models require rather specific conditions such as metal-free gas and strong irradiation by ultraviolet (UV) in the Lyman–Werner (LW) bands (e.g., Wise et al. 2019; Sullivan et al. 2025).

Another established SMBH seeding mechanism involves runaway collisions in dense star clusters undergoing core collapse, particularly in the core of nuclear

E-mails: \*g.fred@columbia.edu (FABG), †ricotti@umd.edu (MR)

star clusters (NSCs), which are some of the densest known stellar systems with surface densities upwards of  $10^6 \text{ M}_\odot \text{ pc}^{-2}$  (see review by Neumayer et al. 2020). NSCs can be triggered to collapse by sudden gas inflows from the surrounding galaxy (Davies et al. 2011), leading to the formation of an intermediate-mass ( $\sim 10^{3-4} \text{ M}_\odot$ ) SMBH seed via stellar collisions (Katz et al. 2015) or black hole mergers (Kritos et al. 2024). Bellovary (2025) recently suggested that LRDs may result from tidal disruption events in collapsing star clusters, connecting SMBH seed formation to star formation. Recent observations highlight this possibility: LRDs have distinct v-shaped spectral energy distributions (SEDs) that turn over at the Balmer limit, suggesting ongoing star formation (Kokorev et al. 2024b; Setton et al. 2024).

In Garcia et al. (2023) (hereafter G23), we examined how different star formation efficiencies (SFEs) in star-forming clouds influence the formation, demographics, and survival of Pop II star clusters in a  $z > 6$  galaxy. Here, we build on that work by adopting an SFE prescription based on high-resolution simulations of gravoturbulent molecular clouds presented in He et al. (2019). Our goal is to track realistic star cluster formation in a typical high- $z$  dwarf galaxy – of which are most responsible for reionizing the Universe (Atek et al. 2024) – and while doing so, outline a pathway for NSC formation. Future work will extend these simulations to explore SMBH seed formation in NSCs.

This paper is structured as follows: Section 1 details our astrophysical models and numerical methods, Section 2 presents our findings, and Section 3 discusses their implications. We summarize our conclusions in Section 4.

## 1. METHODS AND SIMULATIONS

We use a branched version of the adaptive mesh refinement (AMR) code RAMSES-RT (Teyssier 2002; Rosdahl et al. 2013). This radiative hydrodynamics (RHD) code employs a fast, moment-based approach to solve the radiative transfer equations on AMR grids using the M1 closure relation (Rosdahl et al. 2013). Our version of the code contains astrophysical modules developed and implemented from past studies of reionization-era galaxies (Kimm et al. 2017; Katz et al. 2017), star formation in isolated molecular clouds (He et al. 2019, 2020), and Pop III star formation (Park et al. 2021a,b, 2023, 2024). Most recently, we used this code to investigate the effects of UV feedback on the formation of Pop III stars in primordial halos and its transition to Pop II stars in the first galaxies (Sugimura et al. 2024). Many of the numerical methods and physical models are identical to those introduced in G23 and Sugimura et al. (2024). Please refer to these papers for specific details of the initial conditions, gas chemistry, and cell refinement strategy. Here, we review key features of the simulations and highlight improvements made to our star-formation model.

We run a cosmological ( $h = 0.70$ ,  $\Omega_b = 0.044$ ,  $\Omega_m = 0.27$ , and  $\Omega_\Lambda = 0.73$ ) zoom-in simulation on a dark matter (DM) halo that grows to become a dwarf galaxy with stellar mass  $\sim 10^{10} \text{ M}_\odot$  by  $z = 0$ . This halo is in a  $(300 h^{-1} \text{ cMpc})^3$  refined region part of a larger  $(35 h^{-1} \text{ cMpc})^3$  box. We evolve this halo from initial conditions generated at  $z = 127$  with MUSIC (Hahn & Abel 2011) to  $z \sim 8.0$  (note, however, that this varies

slightly depending on the star formation model used, see Section 2). Using AMR, we require all cells in our zoom-in region (with initial refinement level  $l = 14$  and  $800 \text{ M}_\odot$  DM mass resolution) to be refined if they contain: (i) more than 8 DM or star particles or (ii) a gas mass exceeding  $160 \text{ M}_\odot$ , which is around eight times the initial mean gas mass per cell in the refined region. We also use a Jeans criterion; see G23 for additional details. Using this scheme, we achieve a maximum refinement level of  $l = 25$ , corresponding to a minimum spatial resolution of  $\Delta x_{\min} = 0.15[(1+z)/10]^{-1} \text{ pc}$ .

### 1.1. Star formation and feedback

We form stars in maximally refined ( $l = 25$ ) cells when the gas density reaches the critical density threshold:

$$n_{\text{H,crit}} = (5.0 \times 10^4 \text{ cm}^{-3}) \left( \frac{T}{100 \text{ K}} \right) \left( \frac{1+z}{10} \right)^2 \times \left( \frac{N_{\text{cr}}}{4} \right)^{-2}, \quad (1)$$

where  $T$  is the temperature and  $N_{\text{cr}}$  is a free parameter that ensures that the Jeans length  $\lambda_J$  is resolved with  $N_{\text{cr}}$  cells at the maximum refinement level:  $\lambda_J = N_{\text{cr}} \Delta x_{\min}$ . We adopt a fiducial value of  $N_{\text{cr}} = 4$  for our simulations. Once the density of any given cell  $n_{\text{H}} > n_{\text{H,crit}}$ , star formation is treated in a sub-grid manner depending on the metallicity  $Z$  of the cell.

#### 1.1.1. Star formation prescription

We adopt a metallicity threshold  $Z_{\text{crit}} = 10^{-5} Z_\odot$  (with  $Z_\odot = 0.02$ ) that determines whether we form a Pop III system or Pop II star cluster. If  $Z < Z_{\text{crit}}$ , we form a single particle with mass  $120 \text{ M}_\odot$ , representing a Pop III binary system consisting of a 40 and  $80 \text{ M}_\odot$  star. Otherwise ( $Z \geq Z_{\text{crit}}$ ), we form a Pop II star cluster centred on the cell, consisting of individual massive star particles with masses  $m_* = 10 \text{ M}_\odot$ . To do this, we identify all cells with  $n_{\text{H}} > n_{\text{H,crit}}$  and then construct spherically-averaged one-dimensional (1D) gas density profiles on the fly, centred on the peak density  $n_{\text{peak}}$ , which is analogous to a core density. The size of the cloud ( $r_{\text{cloud}}$ ) is defined as the radius at which the 1D profile reaches a cut-off density of  $n_{\text{cut,cloud}} \equiv N_{\text{cut}}^{-1} n_{\text{peak}}$ , where we use a fiducial value of  $N_{\text{cut}} = 10$  in our simulation. From this radius, we can determine the mass ( $M_{\text{cloud}}$ ), average density ( $n_{\text{cloud}}$ ), and average metallicity ( $Z_{\text{cloud}}$ ) of the cloud. Note that Sugimura et al. (2024) adopts different thresholds due to lower resolution and convergence requirements.

Within  $r_{\text{cloud}}$ , we instantaneously form stars in regions with densities  $> n_{\text{cloud}}$  in a randomly distributed manner weighted by the gas density (i.e., a star is more likely to be formed in a denser part of the cloud), since the star formation timescale is typically  $\lesssim 1 \text{ Myr}$  in high-density molecular clouds (He et al. 2019), characteristic of the high- $z$  Universe (Adamo et al. 2024a). Moreover, thermal feedback from Type II supernovae (SNe) occurs on timescales of  $\geq 4 \text{ Myr}$  and the gas densities in our clouds are high enough to be optically thick for radiation to penetrate and affect neighbouring, unresolved stellar cores that form concurrently. The star cluster formed

has a mass of  $m_{\text{star cluster}} = f_* M_{\text{cloud}}$ , where we adopt a total star formation efficiency of the star-forming cloud:

$$f_* = 0.004 \left( \frac{Z_{\text{cloud}}}{10^{-3} Z_{\odot}} \right)^{0.25} \left( \frac{M_{\text{cloud}}}{10^4 M_{\odot}} \right)^{0.4} \times \left( 1 + \frac{n_{\text{cloud}}}{n_0} \right)^{0.91}, \quad (2)$$

with a maximum value of  $f_* = 0.90$  and  $n_0 = 100 \text{ cm}^{-3}$ . This sub-grid model for SFE ( $f_*$ ) is derived from a suite of high-resolution (AU-scale), radiative magneto-hydrodynamic (RMHD) simulations of star formation in isolated molecular clouds conducted by [He et al. \(2019\)](#).

All the stars formed in a given cloud have the same metallicity  $Z_{\text{cloud}}$  and therefore can be treated as a single stellar population (SSP). As we will discuss later in this paper (Section 2.3.3), this is a rather approximate treatment since molecular clouds are hierarchical structures that have inhomogeneous metallicities ([Chevance et al. 2020](#); [Mondal & Chattopadhyay 2024](#)).

### 1.1.2. Radiative and thermal feedback from stars

Our simulations follow the evolution of radiation emitted from stars in four frequency bins: H<sub>2</sub>-dissociating far-UV (FUV) LW radiation ( $11.2 \text{ eV} < h_p \nu < 13.6 \text{ eV}$ ); H I ionizing extreme-UV (EUV) ( $13.6 \text{ eV} < h_p \nu < 24.6 \text{ eV}$ ); He I ionizing ( $24.6 \text{ eV} < h_p \nu < 54.4 \text{ eV}$ ); and He II ionizing ( $54.4 \text{ eV} < h_p \nu < 200 \text{ eV}$ ) radiation. In the Pop III star systems, the  $40 M_{\odot}$  star emits UV radiation for 4 Myr before undergoing a supernova ([Schaerer 2002](#)) which injects  $E_{\text{SN,PopIII}} = 3 \times 10^{52} \text{ erg}$  in thermal energy and releases ejecta with mass  $M_{\text{ejecta,PopIII}} = 20 M_{\odot}$  (of which  $M_{\text{metal,PopIII}} = 9 M_{\odot}$  are metals) into the surrounding gas. The  $80 M_{\odot}$  star directly collapses, feedback-free, into a black hole ([Wise et al. 2011](#)). Though the remnant of this Pop III binary can either form a BH binary or merge to form a single BH, both cases are numerically represented by a  $100 M_{\odot}$  BH particle. Although this particle produces no feedback in the form of X-ray radiation and jets, BH accretion – which we model using the Bondi-Littleton-Hoyle formalism ([Bondi 1952](#)) – can emit negligible UV radiation in our simulations. Furthermore, these BHs grow very little given that they are in low-density environments resulting from the supernova explosion preceding their formation ([Sugimura et al. 2024](#)).

Although we do not directly sample an initial mass function (IMF) for the Pop II masses (recall that  $m_* = 10 M_{\odot}$ ), individual Pop II particles emit UV radiation based on their age and metallicity following the radiative yields for LW, H-ionizing, and He-ionizing radiation ([Kimm et al. 2017](#); [Katz et al. 2017](#)) assuming a Salpeter IMF (1 -  $100 M_{\odot}$ ) ([Salpeter 1955](#)). The Salpeter IMF is also used to calculate SNe yields from the star clusters, with each Pop II SNe (we expect around 1 per  $100 M_{\odot}$  in stars) injecting thermal energy  $E_{\text{SN,II}} = 10^{51} \text{ erg}$  stochastically 4 – 40 Myr since the formation of the star cluster ([Leitherer et al. 1999](#)).

Of course, there are caveats to the astrophysical models we have discussed thus far. For example, our current Pop III sub-grid model is rather simplistic: it does not capture the multiplicity, orbital architectures, and mass function that recent theoretical works have sug-

gested for these first stars (e.g., [Sugimura et al. 2020](#); [Costa et al. 2023](#); [Park et al. 2023](#); [Sugimura et al. 2023](#)). Furthermore, the Pop II star clusters consist of massive,  $10 M_{\odot}$  star particles which significantly impact their secular evolution. This choice, made due to computational cost, can affect the orbital relaxation of low-mass ( $m_{\text{star-cluster}} \lesssim 10^3 M_{\odot}$ ) star clusters and cause them to undergo core collapse and hence evaporate artificially early ([Spitzer 1987](#)). In addition, while we stochastically sample the thermal feedback for core-collapse SNe for the Pop II star clusters, recent studies suggest that different IMF sampling methods can affect the overall stellar mass yields as well as metal enrichment of the ISM in dwarf galaxies ([Applebaum et al. 2020](#); [Jeon & Ko 2024](#)).

## 2. RESULTS

We present the results of a new simulation that builds on the high-SFE (HSFE, with constant  $f_* = 0.70$ ) and low-SFE (LSFE,  $f_* = 0.35$ ) runs first introduced in [G23](#). In our previous work, the two values for  $f_*$  were chosen as lower and upper limit roughly bracketing values expected from [He et al. \(2019\)](#), based on the masses and densities of star-forming gas clouds in our simulations. This initial study was, in part, intended as a controlled numerical experiment to test the dependence of star cluster demographics on the choice of the sub-grid  $f_*$ .

The new simulation presented here is not just a numerical experiment. Rather, it aims to reproduce, with the best fidelity, star formation in a typical dwarf galaxy at high- $z$  by adopting values for the  $f_*$  derived from AU-scale RMHD simulations of star formation in molecular clouds ([He et al. 2019](#)). In the new run (VSFE), the sub-grid SFE varies per cloud, depending on its metallicity, mass, and density (see Eq. 2 for the sub-grid  $f_*$  model). Moreover, the HSFE and LSFE simulations analysed here incorporate updated data from continuing the simulations to lower redshift.

Figure 1 shows a snapshot of the VSFE simulation at  $z = 9.69$ , depicting the galaxy’s star cluster population and gas properties about 20 Myr after a starburst at  $z \sim 9.7^1$ . The stars are shown by their post-processed rest-frame UV ( $\lambda = 1500 \text{ \AA}$ ) surface brightness using values from Starburst99 ([Leitherer et al. 1999](#)) tables assuming a Salpeter IMF between 1- $100 M_{\odot}$  and metallicity  $Z = 10^{-3} Z_{\odot}$ , similar to the procedure outlined in [G23](#).

The first surprising result evident from the galaxy morphology in Figure 1 is that the majority of the stars in the galaxy appear concentrated in a few compact, massive star clusters in the VSFE model. This is more so the case even when compared to the HSFE simulation (see Figure 12 in [G23](#) for reference), which assumes that all stars form with a high SFE of 70%. Later (Section 2.3.1), we quantify the star cluster mass function (CMF) slope and maximum mass. But qualitatively, these star clusters suggest that the VSFE run has a flatter power-law slope ( $\Gamma \sim -0.5$ ) and higher truncation mass ( $m_{\text{CMF, trunc}} \sim 10^5 M_{\odot}$ ). Therefore when making a *realistic assumption* on the sub-grid SFEs in molecular clouds, we still find that galaxies at  $z \gtrsim 10$  form *most of their stars in bound star clusters*. Note that although not fully molecular, the star-forming clouds in this simu-

<sup>1</sup> animated figure available at <https://fred144.github.io/vids>



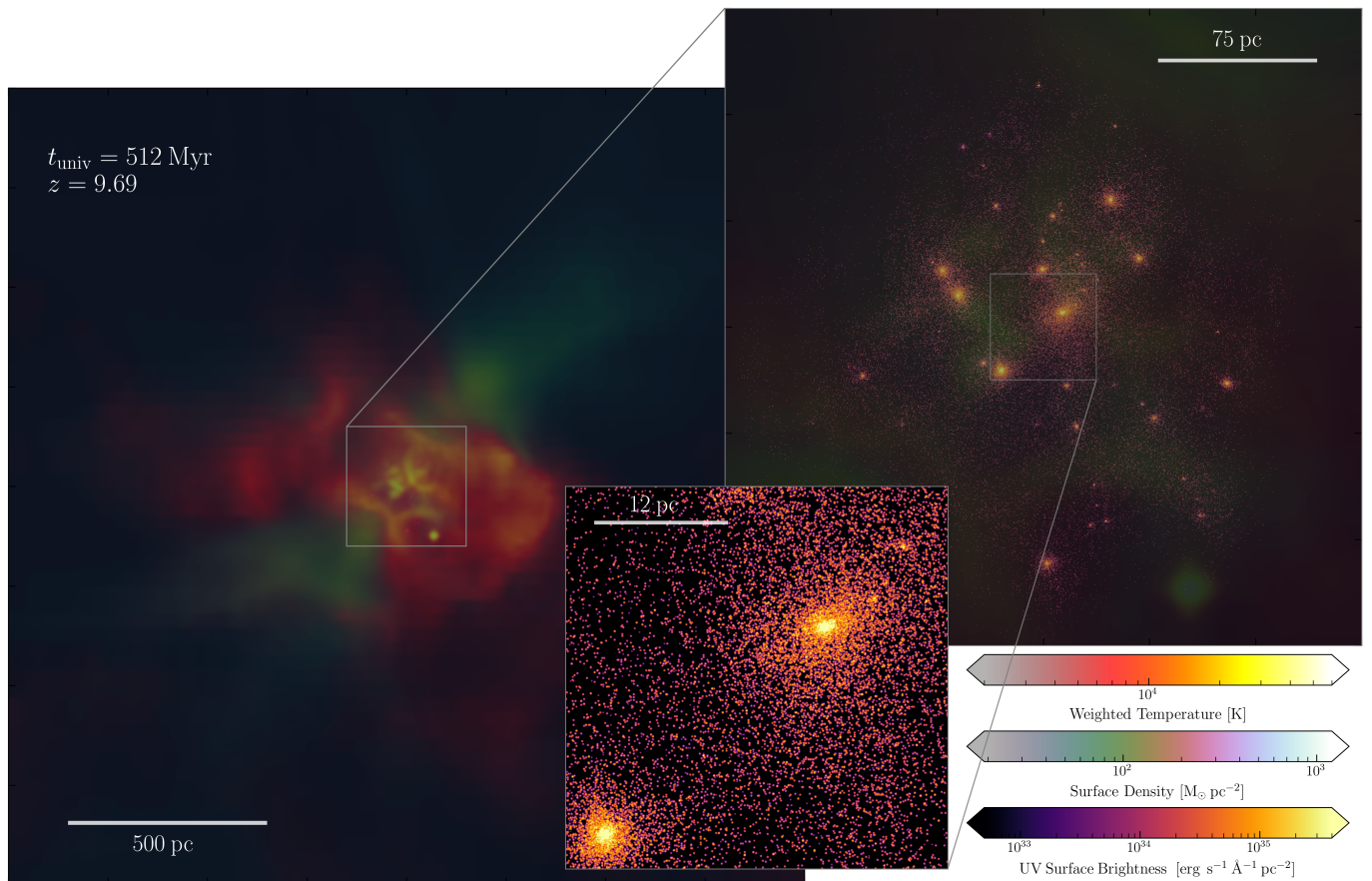


FIG. 1.— Snapshot of a dwarf galaxy simulation at high redshift with realistic SFE in gas clouds derived from AU-scale simulations of star formation, shown just after starburst (a) in Figure 2. The star clusters are shown according to their rest-frame UV surface brightness (at  $\lambda = 1500\text{\AA}$ ) assuming a Salpeter IMF and a metallicity of  $10^{-3} Z_{\odot}$  using Starburst99. The green hues show the gas density while the redder hues show the density-weighted gas temperatures; the colour bars are at the bottom right of the figure. The panels progressively zoom into the star clusters (scale bars shown in physical units), with the bottom panel showing two of the most massive star clusters. The most massive star cluster, shown near the top right corner of the inset, comprises roughly 10% of the galaxy’s total stellar mass.

lation serve as high- $z$  analogues to local molecular clouds and we use these terms interchangeably.

The analysis of simulation results is structured as follows. We begin by taking a look at the galaxy-wide star formation history in this VSFE run from  $z \sim 12.8 - 8.0$ , comparing it with the HSFE and LSFE in Section 2.1. Then in Section 2.2, we analyse the metallicity and SFE evolution of the star-forming clouds throughout the simulations. Narrowing our focus to our most realistic VSFE model, we characterize the population of star clusters produced and their internal properties in Section 2.3. Finally, we present a possible formation scenario for an NSC at high- $z$  in Section 2.4.

### 2.1. Bursty star formation histories

Although the SFEs in the molecular clouds in the VSFE run are mostly  $< 70\%$  (see Section 2.2), the total mass in Pop II stars formed at  $z < 10$  is nearly twice that of the HSFE run, as shown in the top panel of Figure 2. Star formation appears more stochastic, with longer quiescent periods followed by stronger bursts (Fig. 2, bottom three panels). We previously found in G23 that the total mass in stars at a given time – and hence the mass of metals – was nearly independent of the assumed sub-grid  $f_*$  due to self-regulation (e.g., Ricotti 2002; Yajima et al. 2017). However, by adopting the VSFE model, the total

stellar mass formed in the galaxy varies. This suggests that the level of self-regulation depends non-trivially on the star formation and feedback recipe.

Note, the DM halo mass of this galaxy is about  $10^8 M_{\odot}$  at  $z \sim 10$ . This is a typical-mass galaxy at this redshift, having a stellar mass comparable to, or slightly lower than, the faintest galaxies observed by JWST at similar redshifts. A rarer, more massive halo would yield higher stellar masses and thus higher peak star formation rates during major bursts. However, here we focus on the physics of star formation by comparing the properties of the same galaxy when changing the sub-grid recipe for star formation.

The VSFE run produces the most mass in stars. Figure 2 (top panel) shows that the VSFE, HSFE, and LSFE produced (Pop II) stellar masses  $M_{\star} = 1.4 \times 10^6$ ,  $M_{\star} = 9.5 \times 10^5$ , and  $M_{\star} = 7.6 \times 10^5 M_{\odot}$ , respectively. In the lower panels, we show the star formation rate (SFR) for each simulation sampled in 1 Myr bins and show that the VSFE simulation roughly doubles the peak SFR ( $\text{SFR} \sim 0.12 M_{\odot} \text{ yr}^{-1}$  at 475 Myr) of the HSFE simulation ( $\text{SFR} \sim 0.06 M_{\odot} \text{ yr}^{-1}$  at 672 Myr) and is four times higher than that of the LSFE simulation ( $\text{SFR} \sim 0.025 M_{\odot} \text{ yr}^{-1}$  at 422 Myr). Note, the HSFE and LSFE star formation histories extend those initially



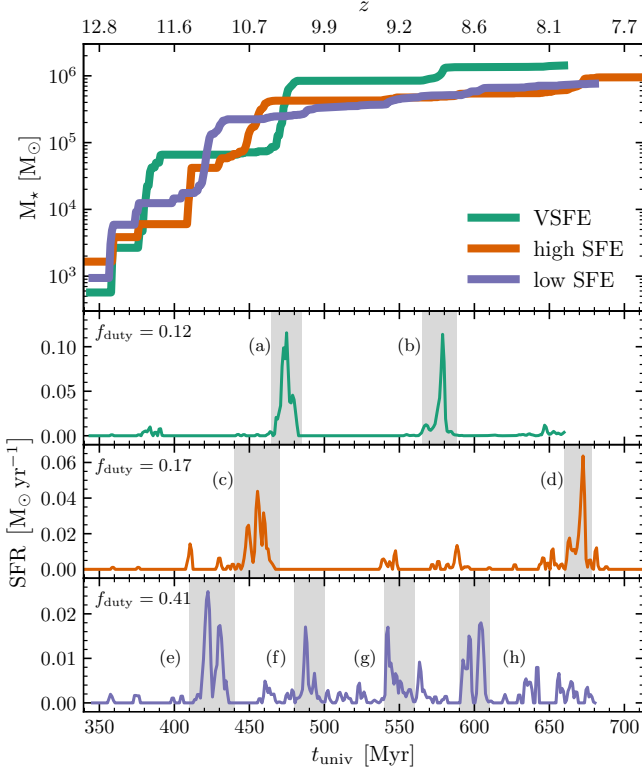


FIG. 2.— Pop II star formation histories of the simulations presented in this paper (see also Fig. 2 (left) in G23). The top panel shows the mass of stars produced under the different assumed star formation efficiencies throughout each simulation (see legend). The following panels (top to bottom) show the corresponding star formation rates (same colours as the legend) in 1 Myr bins. In the top left of each panel, we show the duty cycle  $f_{\text{duty}}$  of star formation, defined as the ratio between times when the SFR  $> 5\%$  of the peak SFR, and the total time elapsed since the onset of Pop II star formation through the end of each simulation run. Note that we also label starbursts (a) - (h) across all simulations, shading regions where the SFRs roughly reach at least 5% of the peak SFR during the starburst. We will use these in the text to refer to star-forming periods (e.g., starburst (a) and (b) for the first and second starbursts in the VSFE model, respectively).

depicted in G23, Figure 2. For example, we show an additional starburst – starburst (d) – in the HSFE galaxy.

We also calculate the duty cycle ( $f_{\text{duty}}$ ), defined as the ratio between the times when the galaxy SFR  $> 5\%$  of its peak SFR and the total time elapsed for Pop II star formation. The  $f_{\text{duty}}$  for the VSFE run is the lowest out of the three at  $f_{\text{duty,VSFE}} = 0.12$ , as opposed to  $f_{\text{duty,HSFE}} = 0.17$  and  $f_{\text{duty,LSFE}} = 0.41$ . Star formation is even more stochastic using the VSFE model than it is with the HSFE: it is more quiescent in between major starbursts, having fewer small bursts with  $\text{SFR} \gtrsim 0.01 \text{ M}_{\odot} \text{ yr}^{-1}$  (Figure 2, grey regions) while also having the highest peak SFR.

Following the arguments in G23 and Sugimura et al. (2024), clouds that form after SFBs require higher masses for gravitational instability (e.g., see G23 Eq. 4) and densities for cooling via self-shielding in a metal-poor environment. Adopting an SFE model that depends on the mass and compactness of the clouds has the effect of boosting starbursts resulting from a few massive clouds and suppressing smaller star-forming episodes arising from lower mass and density clouds.

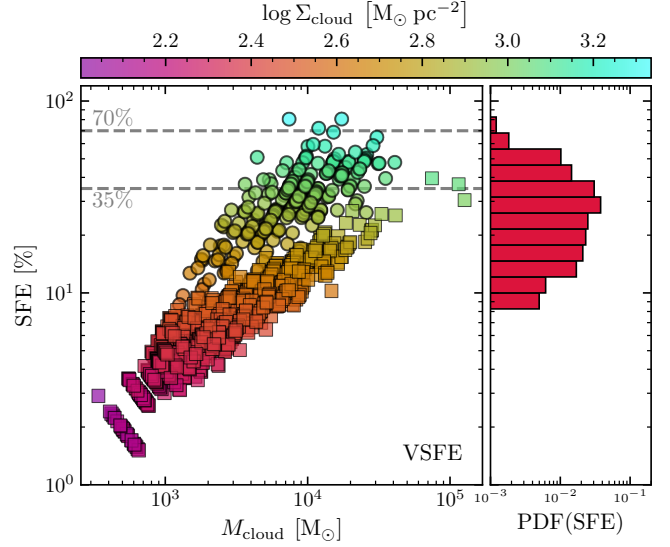


FIG. 3.— SFEs for the star-forming clouds in the VSFE simulation as a function of cloud mass. The *circle* markers are clouds that produced star clusters before starburst (b) ( $t \lesssim 500 \text{ Myr}$ ) while the *square* markers are for clouds that formed stars during and after starburst (b). The markers themselves are coloured by the mean cloud surface density  $\Sigma_{\text{cloud}}$  assuming a spherically symmetric, constant-density cloud. For comparison, we also show two dashed lines indicating the two constant efficiency runs: low SFE (35%) and high SFE (70%). The right panel shows the distribution of SFEs for these two time periods: red for the first and green for the second. Note that the highest SFE achieved by the densest cloud is around 80%, roughly 10% higher than the high-efficiency fiducial run.

In part, the VSFE model allows the galaxy to accumulate a gas reservoir leading up to the burst. This increase in mass and density leads to higher SFEs during starburst in our simulations (Eq. 2). This non-linear effect is reflected in both the total stellar mass and the star-formation histories: the VSFE simulation has two strong SFR peaks and all its minor star-forming periods are suppressed. The stochasticity of star formation observed here can have important implications on the observations of UV-bright objects at high- $z$  (Pallottini & Ferrara 2023; Kravtsov & Belokurov 2024; Vikaeus et al. 2024).

## 2.2. Star formation efficiency of clouds

Figure 3 shows the SFE of each cloud as a function of  $M_{\text{cloud}}$  in the VSFE simulation. The two simulations presented in G23, which assumed cloud-scale star formation efficiencies to be 35% and 70%, are shown as dashed lines. Although the markers are coloured according to the cloud gas surface densities ( $\Sigma_{\text{cloud}} \approx M_{\text{cloud}}/\pi r_{\text{cloud}}^2$ ), recall that the cloud core densities can exceed  $\Sigma_{\text{cloud}}$ . We also distinguish the points (and distributions) according to whether they are formed before (circles, red distribution) or during and after starburst (b) (squares, green).

Looking at the log probability distribution function (PDF) in the right panel of Figure 3, early star formation generally occurs at efficiencies between 10 to 80% in clouds with surface densities reaching as high as  $\Sigma_{\text{cloud}} \sim 2.2 \times 10^3 \text{ M}_{\odot} \text{ pc}^{-2}$  ( $n_{\text{cloud}} \sim 4.8 \times 10^4 \text{ cm}^{-3}$ ). We observe that the highest SFE cloud, although not the most massive throughout the simulation (at only  $M_{\text{cloud}} \sim 2 \times 10^4 \text{ M}_{\odot}$ ), is one of the densest and forms

a  $\sim 5 \times 10^3 M_\odot$  star cluster at 80% SFE during starburst (a). Similarly, we observe that three of the densest clouds form stars at efficiencies exceeding the 70% efficiency assumed in the HSFE model.

Cloud-scale SFEs before starburst (b) are reasonably bracketed by the LSFE and HSFE models, with roughly half falling in this range. However, the range of cloud SFEs during and after starburst (b) ranges between  $\sim 2\text{--}40\%$ , with the majority having efficiencies  $< 35\%$ , lower than what is assumed in the LSFE model. The SFEs are also closely tied to the SFRs observed in Figure 2. In the HSFE model, the SFE is high even before reaching the peak of starburst (a), which has the consequence of suppressing star formation and reducing the peak SFR. Conversely in the LSFE model, the SFE is assumed to be low even at peak bursts reducing the peak SFR.

A notable observation is that the most massive clouds ( $M_{\text{cloud}} \sim 10^5 M_\odot$ ) form stars during starburst (b). This is consistent with the findings in Sugimura et al. (2024) and the argument presented above in Section 2.1, where higher masses are needed for clouds to become gravitationally unstable and form stars at low metallicities and high temperatures from preceding star formation, which provide thermal support.

### 2.2.1. Metallicity evolution of star-forming clouds

The trends observed in Figure 3 are partly explained by the metals produced by SNe in starburst (a), which enrich the ISM and lead to higher metallicity clouds during starburst (b). This becomes clearer when we turn our attention to Figure 4, which shows the relationship between  $Z_{\text{cloud}}$  and  $M_{\text{cloud}}$  for each simulation (see the bottom right of the left panels for each corresponding run). The right panels show the shape of the metallicity function:  $dN/d\log(Z_{\text{cloud}}/Z_\odot)$  at the end of each simulation, while the very bottom row shows the mass function of the clouds in all three simulations overlaid on top of another. We also colour each marker by the star cluster formation time in the simulation. Recall from Section 1.1.1 that the metallicities of individual Pop II stars formed are equal to  $Z_{\text{cloud}}$ . Hence,  $Z_{\text{cluster}} = Z_{\text{cloud}}$  in many cases – especially at the formation of a Pop II star cluster. However, a cluster may contain multiple populations due to mergers. Also, this is not to be confused with  $Z_{\text{PopII}}$  which is the metallicity of *individual stars* and may not necessarily belong to the same (or any) star cluster throughout the simulation.

For all simulations, the lowest metallicity cloud ( $Z_{\text{cloud}} \sim 8 \times 10^{-4} Z_\odot$ ) forms at  $z = 12.95$  ( $t_{\text{univ}} \sim 350$  Myr). This cloud forms a star cluster at  $f_* = 0.22$  in the VSFE simulation, indicating that  $f_* = 0.35$  and  $f_* = 0.70$  both overestimate the efficiency of this cloud. Feedback from this first star cluster heats the surrounding gas, delaying subsequent star-forming periods. And since hotter clouds with negligible metal cooling require larger masses to become gravitationally unstable (Section 2.1), we get a succeeding population of more massive clouds that garner higher SFEs, reaching as high as 80% in our VSFE model. We observe this in all simulations with cloud masses typically reaching around  $2 \times 10^4 M_\odot$  after ( $\lesssim 20$  Myr) the first star cluster forms, see Figure 4. The initial star formation and metal enrichment histories are fairly similar across simulations; adopting the VSFE model has trivial consequences for the star formation immediately

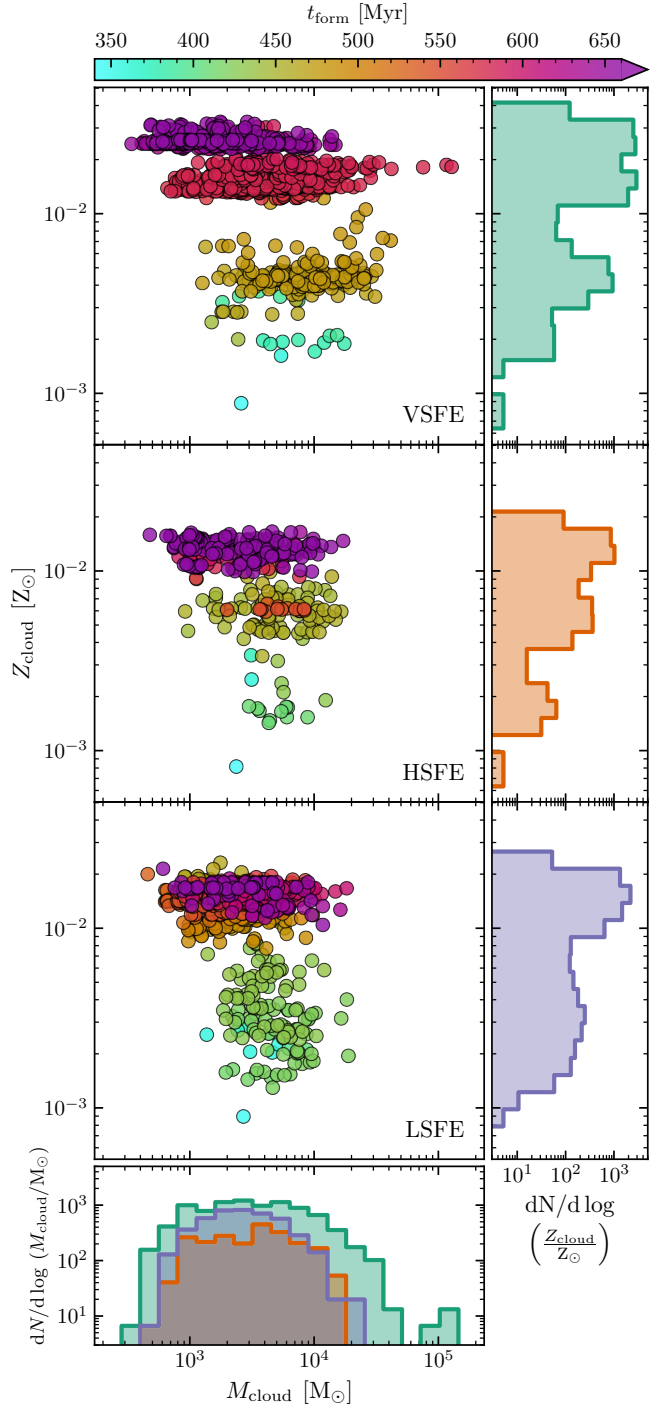


FIG. 4.— We show the Pop II star-forming cloud metallicity as a function of mass for the different star-forming periods (see top colour bar). For each row, the right panel shows the metallicity function for the clouds for a given model (see lower right of each left panel). The very bottom panel shows the mass function of the clouds, coloured according to the sub-grid SFE for each run. Note, that the metallicity of the star clusters is identical to their natal clouds’.

following the first star cluster.

However, realistic SFEs do play an important role during and after starbursts. Namely, they can significantly alter the total stellar masses, which are directly related to a galaxy’s metal production and stellar feedback budgets. These feedback processes impact the next generation of

star formation. Recall from Figure 3 that a significant portion of star formation in the VSFE model during starburst (a) occurs in higher SFE ( $f_* \gtrsim 0.35$ ) clouds due to the compounding feedback from earlier star formation, progressively increasing the SFEs leading up to the burst. Because of this, clouds can reach SFEs as high as 80% during starburst (a). The intense feedback from this high SFE burst leads to complete quiescence which we can see by the large gap ( $\gtrsim 50$  Myr) in  $t_{\text{form}}$  for the top panel in Figure 4. As we saw in G23, more bursty star formation histories exhibit an evident multi-modal metallicity distribution leading to the LSFE model having a comparatively more gradual metal enrichment than the HSFE. Our results here are consistent with this, with the most stochastic model of the three ( $f_{\text{duty,VSFE}} = 0.12$ ) also having the clearest multi-modality (Figure 4, right histograms). In addition to this multi-modality, the VSFE model reaches the highest metallicity among the three runs, despite not evolving this model down to lower redshifts (Figure 2).

We also find that the metallicity evolution of the star clusters is non-monotonic; i.e., lower metallicity clouds may condense in the ISM even after higher metallicity star clusters have already formed. For example, in the VSFE model (Figure 4, top row), there are lower metallicity clouds (orange points,  $\sim 3 \times 10^{-3} Z_{\odot}$ ) that form *after* clouds with higher metallicities (light green) had already formed stars. This also occurs later during and after the second starburst and across the other two models, possibly hinting at metallicity dilution via inflows of more pristine gas (see, Sugimura et al. 2024; Stiavelli et al. 2024) or metallicity inhomogeneities in the ISM before the metals are thoroughly mixed.

The comparatively more intense heating from starburst (a) in the VSFE run leads to the formation of the most massive clouds (bottom row of Figure 4, green) across all models during the following starburst (b), reaching masses of  $M_{\text{cloud}} \gtrsim 10^5 M_{\odot}$ . In comparison, the HSFE and LSFE reach cloud masses of only  $M_{\text{cloud}} \sim 2 \times 10^4 M_{\odot}$ . The general form of the cloud mass function is roughly consistent with a piecewise log-normal and power law, characteristic of a gravoturbulent star-forming environment (Burkhart 2018). The dynamical evolution of the stars produced by these high mass, metal-enriched, lower-density (see Figure 3, colour bar) clouds is discussed in further detail in Section 2.4.

In summary, adopting the VSFE model alters the chemical enrichment history of star-forming clouds by enabling comparatively higher metal yields and thermal feedback budgets than the HSFE and LSFE runs. This allows the formation of higher-temperature, more massive clouds. However, these massive clouds harbour higher metal enrichment which can lead to lower SFEs ( $f_* \lesssim 0.35$ ). Higher metal enrichment can also cause clouds to fragment to lower masses, leading to a transition to low SFEs we see in Figure 3 post starburst (b).

### 2.3. The first star clusters

So far, we have focused on the overall star formation histories across all simulations. In this section, we will shift our attention to the most realistic VSFE model, characterizing the properties of star clusters in the first 700 Myr.

To identify star clusters, we post-process our snapshots with a friends-of-friends (FoF) structure finder Efstathiou et al. (1985), grouping stars that are closer than  $l_{\text{link}} = 10^{-4}$  times the mean separation of all the star particles. For a given star cluster we calculate the total kinetic energy  $E_{\text{kin}} = \frac{1}{2} \sigma_{3D}^2 m_{\text{star cluster}}$ , where  $\sigma_{3D}^2$  is the 3D velocity dispersion of the stars,  $m_{\text{star cluster}}$  is the mass of the Pop II star cluster. We then approximate each clump as a uniform density sphere having total potential energy  $E_{\text{pot}} = -\frac{3}{5} G m_{\text{star cluster}}^2 r_{\text{half}}^{-1}$ , where  $r_{\text{half}}$  is the half-mass radius and  $G$  is the gravitational constant. Knowing that for an object in virial equilibrium:  $2E_{\text{kin}} = -E_{\text{pot}}$ , we can estimate the virial parameter  $\alpha_{\text{vir}} \equiv -2E_{\text{kin}}/E_{\text{pot}}$ . Similar to the commonly used virial parameter for molecular clouds, a cluster found by the FoF is considered to be virialized if  $\alpha_{\text{vir}} \leq 1$  and bound if  $\alpha_{\text{vir}} \leq 2$  (Kauffmann et al. 2013).

However, given that many of our star clusters (especially low mass ones) are not very well resolved due to their sizes being 1-2 pc and the gravitational softening  $\Delta x_{\text{min}} = 0.15$  pc, clumps may be considered as bound star clusters even with  $\alpha_{\text{vir}}$  slightly larger than 2. Furthermore, we require a clump to have a mass  $\geq 300 M_{\odot}$  (corresponding to at least 30 star particles) to be considered as a star cluster.

#### 2.3.1. Star cluster mass functions

We find that the Pop II star CMFs in the VSFE model are well represented by a power law with slopes varying between  $\Gamma \sim -0.3$  to  $-1.1$  depending on the time since a major starburst and whether or not we include unbound star clusters. Figure 5 (top row) shows the CMFs for all identified star clusters (bound and unbound) as hatched histograms and the initial cluster mass functions (ICMFs) as solid histograms. The ICMF is simply the at-birth CMF:  $f_* M_{\text{cloud}}$ ; i.e., right after the star cluster was formed. The ICMF of the VSFE run (Figure 5, solid distributions) is well described by a log-normal distribution:  $f(M_{\text{cloud}}) = a \exp[(M_{\text{cloud}} - \mu)^2 / (2\sigma^2)]$ , with fitted mean ( $\mu$ ) ranging between 2.2 and 3.4, standard deviation  $\sigma \sim 0.5$  to 0.9, and some normalization  $a$ . Given the definition of the ICMF, we expect its shape and extent to be similar to the distribution of  $M_{\text{cloud}}$  depicted in the bottom panel of Figure 4. However, recall that the few massive ( $\sim 10^5 M_{\odot}$ ) star-forming clouds shown in 4 have relatively low SFEs ( $\lesssim 35\%$ ), hence the star clusters produced have maximum at-formation masses of a few  $10^4 M_{\odot}$ .

The CMF is time-dependent due to the dynamical evolution of the star clusters (Figure 5, left to right). For example, star clusters as massive as  $10^5 M_{\odot}$  are formed via mergers since the ICMF shows a maximum at-birth star cluster mass of  $\sim 2 \times 10^4 M_{\odot}$  after the high-efficiency starburst (a) at  $z = 9.9$ . For reference, this star cluster is the main star cluster we zoom into in Figure 1. These massive clusters then lose mass as shown in the second column ( $z = 9.7$ ). In the third and fourth columns ( $z = 8.7 - 8.0$ ), the CMF steepens indicating the formation of predominantly low-mass, unbound star clusters after the low-SFE starburst (b). This is confirmed when filtering for star clusters with  $\alpha_{\text{vir}} \leq 2.5$  (which includes those marginally bound) in the bottom row of Figure 5. This filtering only slightly changes the slope of the



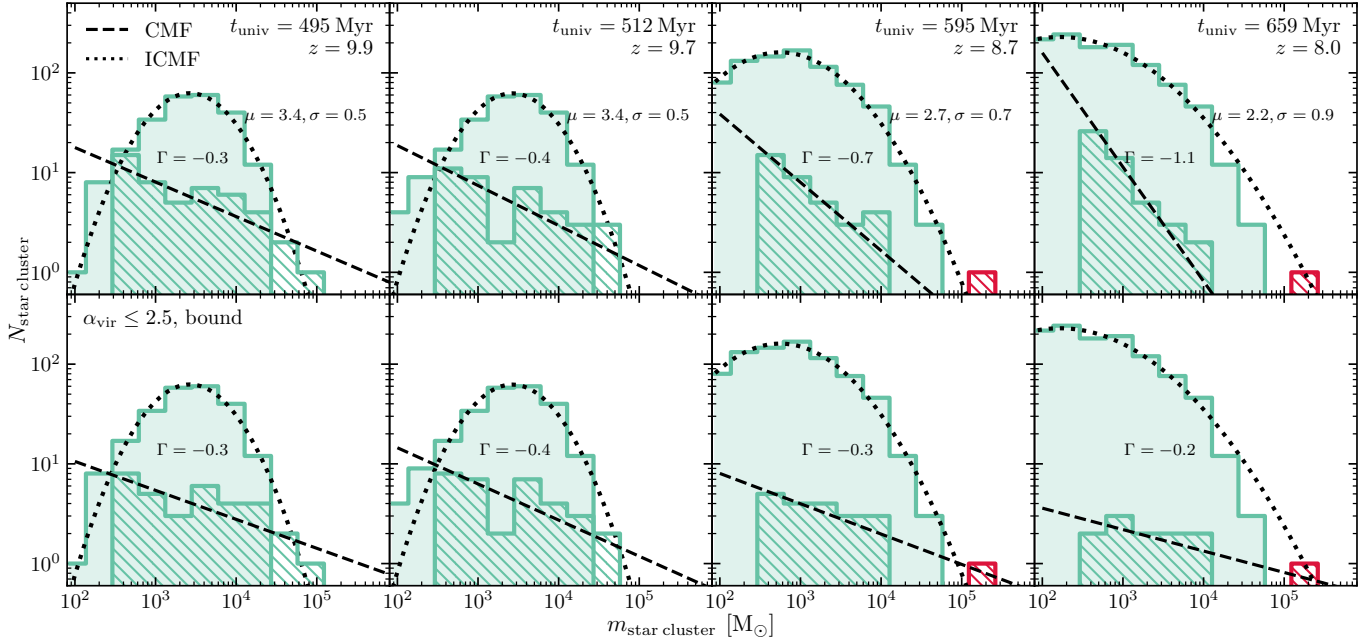


FIG. 5.— At-birth (solid) and current (hatched) star cluster mass function for the VSFE run. The simulation progresses from left to right and we see how the star cluster population evolves after starburst (a) from the first column and second column ( $t_{\text{univ}} = 512$  Myr corresponds to the snapshot shown in Figure 1), right after the second starburst (the third column), and the latest snapshot (fourth column). We also show reference lines for power laws used to fit the CMF with power law index  $\Gamma$  which also evolves. Note that the NSC seeded by the starburst (b) is indicated in red. Furthermore, we show the cumulative ICMF fitted with a Gaussian in log-log space to find the mean ( $\mu$ ) and standard deviation ( $\sigma$ ). The top row corresponds to all the star clusters, both bound and unbound (see text for definition), while the second row only shows those we consider bound.

CMF after starburst (a) (first two columns); however, it significantly alters them post-starburst (b), changing the slope from  $\Gamma = -0.7$  and  $-1.1$  to much flatter values of around  $\Gamma = -0.2$  (bottom right of Figure 5). We can also indirectly see this effect by looking at the mean mass of the ICMF, which decreases between the middle left ( $\mu = 3.4$ ,  $t_{\text{univ}} = 512$  Myr) and middle right ( $\mu = 2.7$ ,  $t_{\text{univ}} = 595$  Myr) panels. This is caused by low-efficiency star formation in highly-fragmented, metal-enriched, and low-mass clouds (Figure 4). These star clusters have at-birth masses of a few  $100 M_{\odot}$  and quickly get disrupted.

### 2.3.2. Seeding of a nuclear star cluster

Coincident with the second burst of star formation is the formation of a  $\sim 10^5 M_{\odot}$  object we highlight in red in the CMFs of Figure 5. This object – which we characterize as an NSC – is grown predominantly through the merger of star clusters formed in lower SFE clouds (see Section 2.4 for a more thorough examination). The initial growth of this object was first facilitated by a  $5 \times 10^4 M_{\odot}$  star-forming cloud during starburst (b).

We further verify the existence of an NSC in Figure 6. The NSC has a mass of  $m_{\text{NSC}} = 2 \times 10^5 M_{\odot}$  in a  $1.4 \times 10^6 M_{\odot}$  galaxy by  $z = 8.0$ . For comparison, we depict nearby nucleated dwarf galaxies in the Fornax and Virgo clusters in the nearby ( $z \sim 0$ ) Universe from the MUSE Fornax3D (Fahrion et al. 2021, 2022) and the ELVES survey (Carlsten et al. 2022). We also depict the NSC-to-galaxy stellar mass scaling relation presented in a review by Neumayer et al. (2020), where the NSC masses were found to scale as  $m_{\text{NSC}} \propto M_{\star}^{1/2}$ . This indicates that NSCs contain a higher fraction of their host galaxy’s mass in lower-mass galaxies. Indeed,

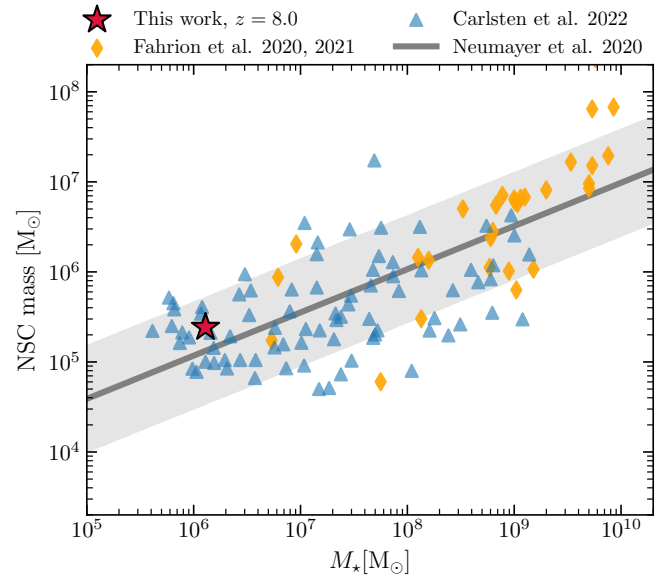


FIG. 6.— Nuclear star cluster mass as a function of host galaxy stellar mass. We compare the properties of the VSFE galaxy at  $z = 8$  (red star) with those compiled for nucleated dwarf galaxies (at  $z \sim 0$ ) from the Multi Unit Spectroscopic Explorer (MUSE) Fornax3D survey (Fahrion et al. 2021, 2022) as well as the Exploration of Local Volume Satellites (ELVES) survey for low-mass early-type galaxies in the Virgo cluster (Carlsten et al. 2022). For comparison, we show the scaling relation presented in a review by Neumayer et al. (2020) (Eq. 1), derived for a sample of 407 NSC and host galaxy masses  $M_{\star} = 10^6$ – $10^{11} M_{\odot}$  along with the scatter around the fit.

the NSC formed in this work hosts roughly 20% of the host galaxy’s stellar mass by  $z = 8.0$ , falling within the 0.6 dex scatter around the expected scaling relation in

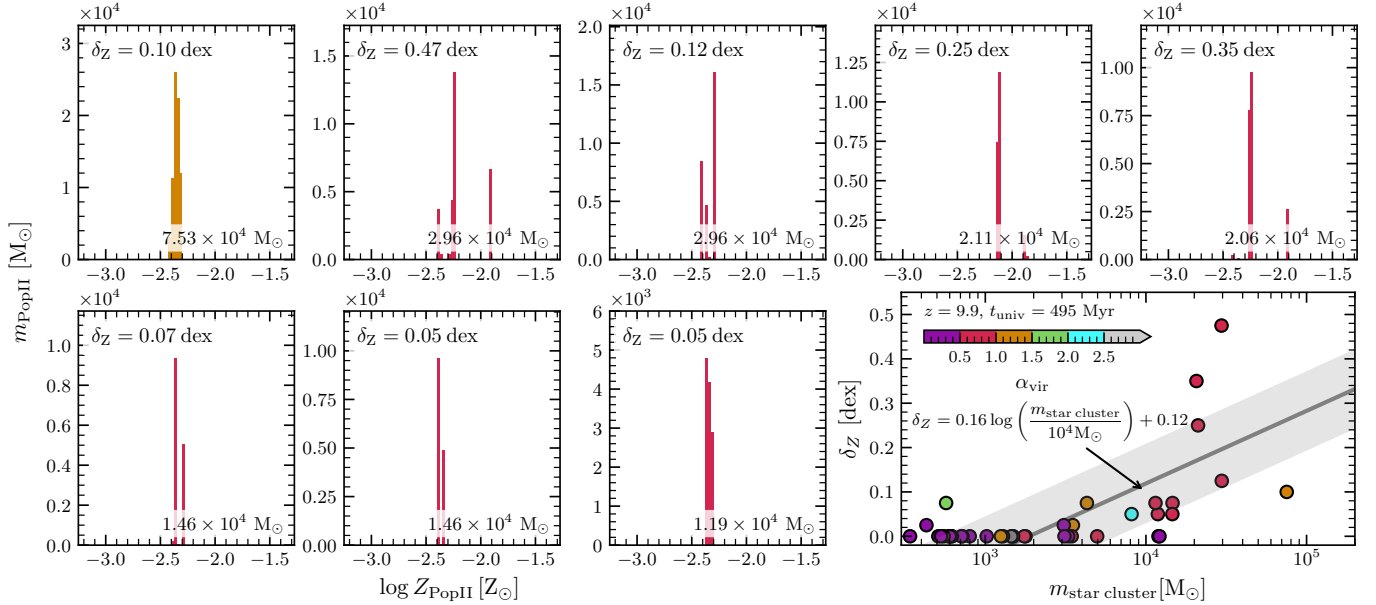


FIG. 7.— Metallicity distribution of Pop II stars in the 8 most massive star clusters in our realistic (VSFE) simulation at  $z = 10$ , immediately after starburst (a). Each panel shows the distribution of Pop II star particle metallicities in a given star cluster (the total cluster mass is shown in each panel), starting with the two most massive in the top left (then across). The distributions are coloured according to  $\alpha_{\text{vir}}$  of the star cluster (see colour bar at the bottom right) and are displayed in log-linear space with 0.025 dex bins. We quantify the metallicity spread in each star cluster ( $\delta_Z$ ) by calculating the range of metallicities from bins with appreciable mass contributions ( $> 10\%$  of the maximum mass in any given bin). In the bottom right panel, we show  $\delta_Z$  as a function of star cluster mass for all identified star clusters, with points coloured by  $\alpha_{\text{vir}}$ . We also show a rough log-linear fit for clusters with  $\delta_Z > 0$  and  $m_{\text{star cluster}} \geq 10^4 M_\odot$ .

Figure 6.

### 2.3.3. Multiple populations in star clusters

Due to the  $m_* = 10 M_\odot$  stellar mass resolution in our simulation, we can roughly trace how the dynamics of star clusters determine their internal stellar populations. Figure 7 looks at this in closer detail by showing the metallicity distributions of Pop II star particles in the most massive star clusters at  $z = 10$ , right after starburst (a). Note that each panel shows the metallicity distribution within a given cluster (with total mass shown in the bottom right).

The most massive star cluster ( $m_{\text{star cluster}} = 6.7 \times 10^4 M_\odot$ ) has a noticeable 0.1 dex scatter in its metallicity distribution, with stars predominantly having metallicities between  $-2.4 < \log(Z_{\text{PopII}}/Z_\odot) < -2.3$  and a negligible population (less than 1% of the total mass) of lower-metallicity stars. We quantify the spread in a star cluster’s metallicities ( $\delta_Z$ ) by binning the log metallicities (0.025 bin sizes), masking out bins with counts  $< 10\%$  of the peak number of star particles in any given metallicity bin (this prevents a relatively small population from artificially increasing the calculated spread), and then taking the range of values. We observe that the most massive star clusters in Figure 7 have  $\delta_Z \sim 0.10 - 0.47$  dex, while clusters with  $m_{\text{star cluster}} \lesssim 10^4 M_\odot$  have less noticeable metallicity spreads  $\delta_Z \lesssim 0.1$ . Figure 7 bottom right shows  $\delta_Z$  for all identified star clusters. There is a weak trend between  $\delta_Z$  and  $m_{\text{star cluster}}$ , best described by the fitted log-linear relationship  $\delta_Z = 0.16(m_{\text{star cluster}}/10^4 M_\odot) + 0.12$  we show in the panel, along with a  $\pm 0.08$  dex uncertainty derived from fitting.

However, we caution the reader that the scatter we present here is spread across chemical species since we currently do not track individual elemental abundances

and enrichment pathways (e.g., AGB stars and Type Ia SNe); much higher model fidelity is needed to address questions about the origins of multiple stellar populations in GCs (Charlie & Spergel 2010; Bastian & Lardo 2018; Bekki 2019; El-Badry et al. 2019). However, this spread suggests that the metallicities of star-forming cloud complexes are non-homogenous and are already patchy even at sub-parsec scales and within the first Gyr of metallicity evolution within galaxies. While these star clusters are formed as an SSP, star formation within a cloud is hierarchical and sub-clumps of slightly different metallicities merge early on to form bound star clusters (the distributions are coloured according to the  $\alpha_{\text{vir}}$ ). While the dependence of metallicity spreads on the star cluster mass has been observed in local GCs with masses  $\sim 10^5 - 6 M_\odot$  by Latour et al. (2025), they can be interpreted in models that include self-enrichment (e.g., see Bailin 2018; McKenzie & Bekki 2021). However, if the star cluster is very compact and not too massive (as in our simulation), we expect that the timescale for self-enrichment is longer than the star formation quenching timescale ( $< 2$  Myr, He et al. 2019). The current metal enrichment scheme we use in our simulation forms stars in each gas clump instantaneously, and only tracks the enrichment of Type II SNe species, dominated by  $\alpha$  elements and some Fe production (Woosley & Weaver 1995; Roberti et al. 2024). Therefore, we interpret the spread seen here as due to inhomogeneities in the gas pre-enrichment rather than self-enrichment. This non-monolithic, hierarchical view of star cluster formation and assembly has been studied at the molecular cloud scale (e.g., Vázquez-Semadeni et al. 2017; Grudić et al. 2022) and here we see a confirmation of this process at galactic scales in the ISM of high- $z$  galaxies.

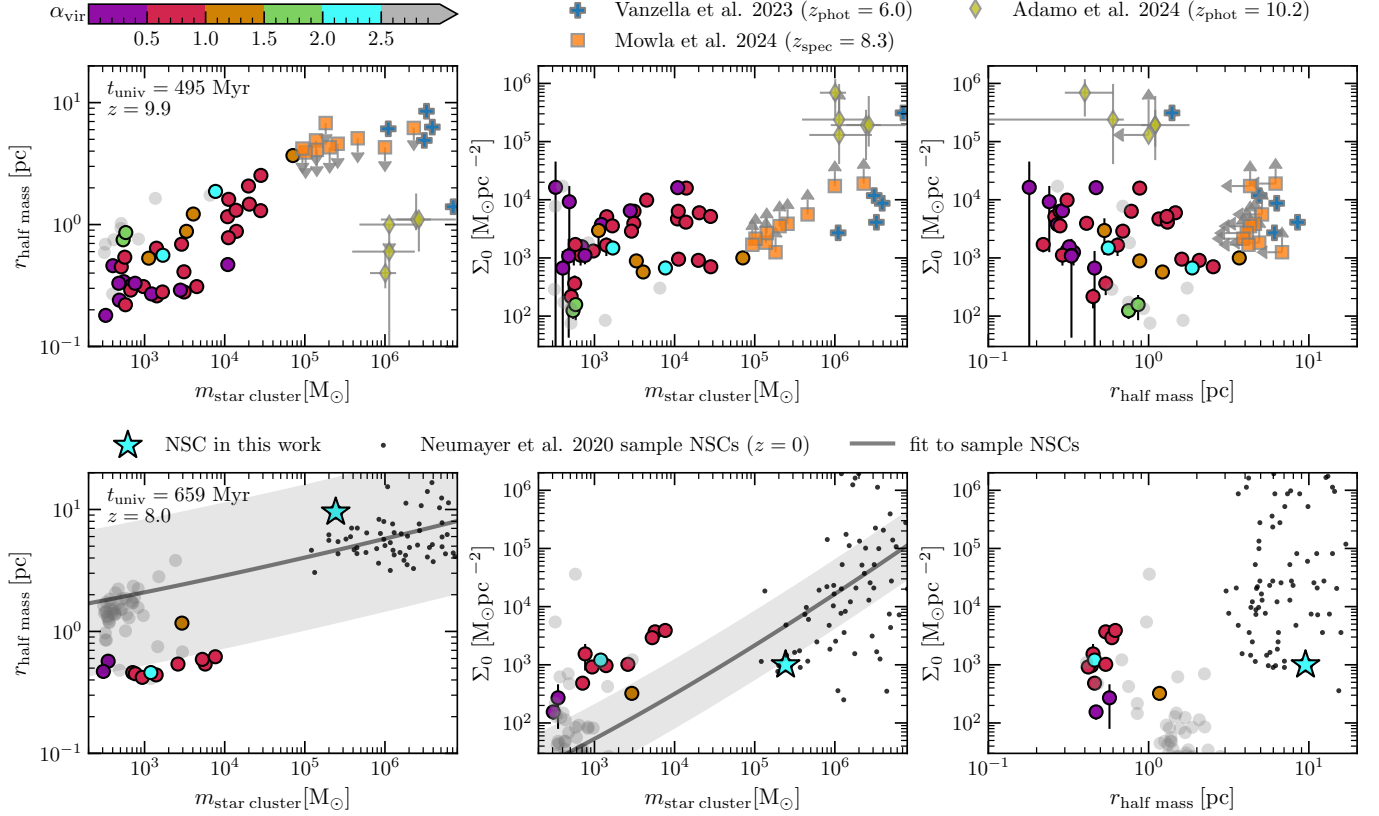


FIG. 8.— The evolution of the mass-radius relation (left column), mass-surface density relation (centre), and radius-surface density relation (right) of star clusters in the VSFE galaxy after starburst (a) ( $t_{\text{univ}} = 495$  Myr,  $\lesssim 20$  Myr since the peak of the burst) and at the end of the simulation ( $t_{\text{univ}} = 659$  Myr, bottom row). The circles are coloured by the virial parameter if marginally bound (has a value of  $\alpha_{\text{vir}} \leq 2.5$ ) and grey otherwise. We also include properties of star clusters from the Sunrise Arc (Vanzella et al. 2023), Cosmic Gems Arc (Adamo et al. 2024b), and Firefly Sparkle (Mowla et al. 2022, 2024) observed through strong lensing at high- $z$  as points of comparison. In the bottom rows, we indicate the NSC formed and the surviving star cluster population at the end of the simulation along with a select sample of NSCs in early and late-type galaxies compiled in a review by Neumayer et al. (2020). We fit the mass-radius and mass-density relation and show the results along with a 0.6 dex scatter (grey band) for reference.

#### 2.3.4. Star cluster masses and sizes

Figure 8 illustrates the star cluster population 20 Myr after starburst (a) at  $z = 9.9$  (top row) and the surviving population by  $z = 8.0$  (bottom row). The left and centre panels show  $r_{\text{half mass}}$  and central surface densities ( $\Sigma_0$ ) as functions of  $m_{\text{star cluster}}$ , while the right panels depict the  $\Sigma_0 - r_{\text{half mass}}$  relation. For comparison, high- $z$  star cluster observations – both photometric (Vanzella et al. 2023; Adamo et al. 2024b) and spectroscopic (Mowla et al. 2024) – are shown in the top row (see respective papers for similar plots). Here,  $\Sigma_0$  is derived by fitting the projected density profile,  $\Sigma(r) = \Sigma_{\text{bg}} + \frac{\Sigma_0}{1 + (r/r_{\text{core}})^\alpha}$ , yielding the background surface density  $\Sigma_{\text{bg}}$ , core radius  $r_{\text{core}}$ , and power-law index  $\alpha$  (King 1962). Errors in  $\Sigma_0$  arise from the non-linear least-squares fit.

After starburst (a), the galaxy predominantly comprises of bound (see colour bar), compact ( $r_{\text{half-mass}} \lesssim 3$  pc), and dense ( $\Sigma_0 \sim 10^{2-4} \text{ M}_\odot \text{ pc}^{-2}$ ) star clusters. However, by the end of the simulation ( $t_{\text{univ}} = 659$  Myr,  $z \sim 8.0$ ), fewer bound star clusters survive and those that do tend to have masses no more than  $m_{\text{star-cluster}} \sim 10^4 \text{ M}_\odot$  and  $r_{\text{half-mass}} \lesssim 2$  pc (second row of Figure 8). The NSC is an outlier, having  $r_{\text{half mass}} \sim 10$  pc and amassing nearly a few  $10^5 \text{ M}_\odot$ . For comparison, the bottom row of Figure 8 also includes properties of nearby

( $z \sim 0$ ) NSCs from Neumayer et al. (2020) as dots in the mass-radius, mass-density, and radius-density planes, along with extrapolated fits (note,  $\Sigma_0$  has a weak dependence on  $r_{\text{half-mass}}$ ). While the NSC’s radius is roughly twice and  $\Sigma_0$  about a quarter of the expected values, it still lies within 0.6 dex of the relationship fitted to NSCs. Furthermore, these trends were fitted for a sample of NSCs at  $z \sim 0$ , while the properties of the NSC and star clusters we show in Figure 8 are at  $z = 8.0$ .

The existence of an NSC significantly impacts the surviving star cluster population. By  $z = 8.0$ , the grey circles in Figure 8 highlight a larger population of unbound clusters compared to the top row. These objects have larger sizes ( $r_{\text{half mass}} \gtrsim 1$  pc), lower masses ( $m_{\text{star cluster}} \lesssim 10^4 \text{ M}_\odot$ ), and lower central densities ( $\Sigma_0 \lesssim 10^3 \text{ M}_\odot \text{ pc}^{-2}$ ), indicative of dynamical perturbations (Kruijssen et al. 2012). Most bound clusters are remnants of starburst (a), as the NSC’s formation creates a tidally crowded environment that disrupts clusters at birth. Additionally, the formation of a centrally dominant object imposes dynamical friction causing star clusters with wider orbits to gradually migrate to the galactic centre, further contributing to the dissolution of the star clusters and further mass growth of the NSC (e.g., see Gao et al. 2024).

The VSFE model captures diverse star cluster popula-



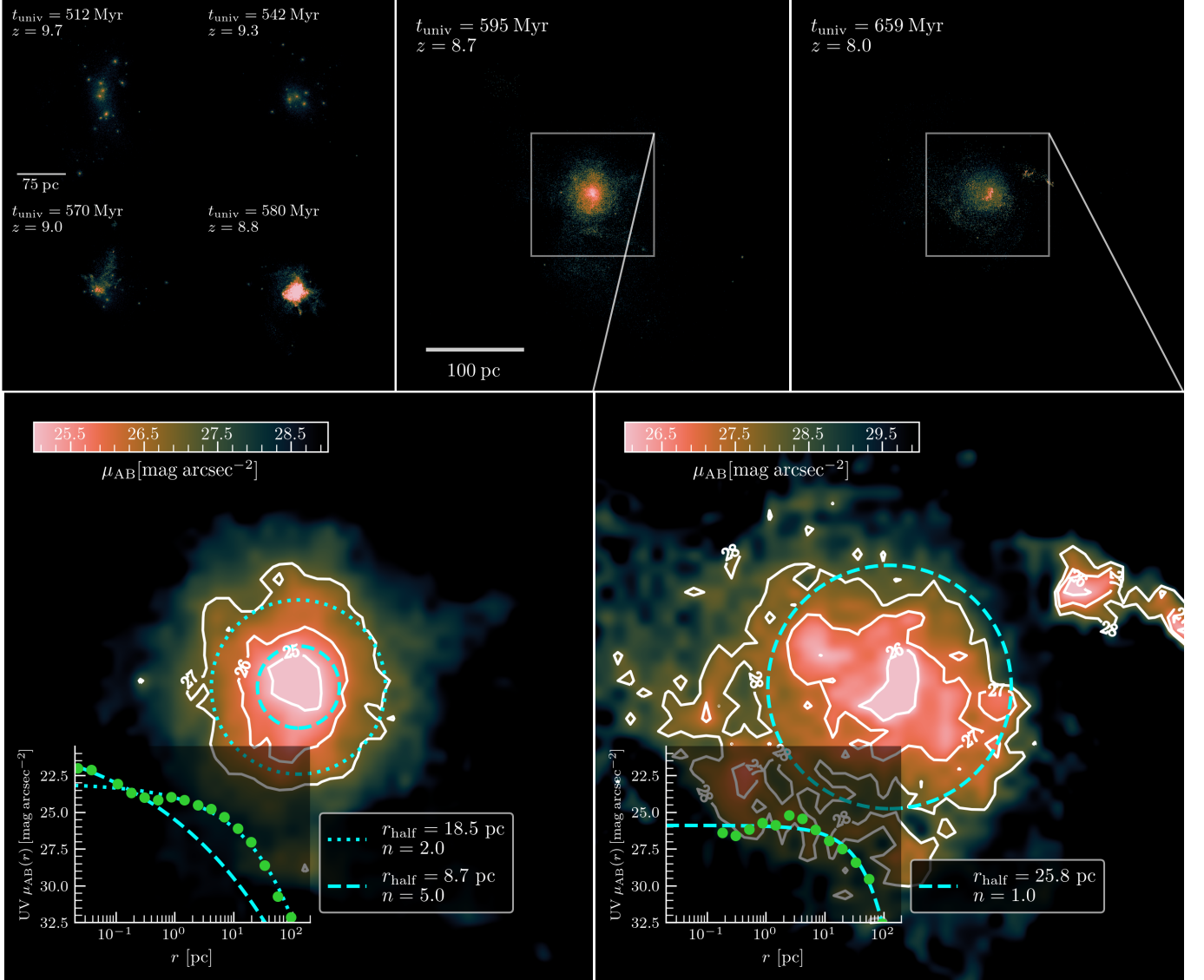


FIG. 9.— A time-lapse of the VSFE galaxy leading up to (top left), during (top centre), and after (top right) the formation of the central NSC, coloured according to the redshift-corrected stellar surface brightness (absolute AB magnitudes at 1500 Å rest-frame). We see the galaxy transition from a star cluster-dominated galaxy to a primarily bulge-dominated one during  $t_{\text{univ}} = 580 - 595$  Myr. We then show a zoomed inset view of the central ( $\sim 100$  pc) region of the galaxy right after the bulge was formed from starburst (b) and its state near the end of the simulation (bottom left and right, respectively). For reference, we show surface brightness contours in these insets along with the half-light radii extracted from fitting the surface brightness of the entire galaxy with Sersic profiles (Eq. 3, see inset of these panels.)

tions, including those (i) nearly  $10\times$  more massive than the largest clusters in the HSFE and LSFE models of G23, formed at higher SFEs ( $\sim 80\%$ ), and (ii) those formed in lower-mass, metal-enriched clouds with SFEs  $< 10\%$ . As star formation in the galaxy transitions from (i) to (ii), we observe the seeding and growth of an NSC.

#### 2.4. Seeding a nuclear star cluster

This section examines the formation of the NSC in detail. Figure 9 presents the observed rest-frame UV surface brightness ( $\mu_{\text{AB}}$ ) of the galaxy. The top left panel shows 200 pc stamps of the star-forming region after starburst (a) when star clusters dominated the galaxy’s light and its  $\sim 80$  Myr evolution leading to starburst (b), which seeds the NSC (top centre). By  $z = 8.0$ , the galaxy morphology (top right) becomes UV-dominated at the centre. The bottom row of Figure 9 provides a detailed view

of the central regions in the top centre and right panels, with surface brightness contours overlaid.

Identifying NSCs is typically ambiguous both observationally and theoretically, especially near the edge cases of the size and mass distributions of NSCs (Neumayer et al. 2020). While the properties of the NSC formed will certainly evolve further (recall, the galaxy in this work is expected to grow into  $10^{10} M_{\odot}$  by  $z = 0$ ), this is where the NSC lies at  $z = 8.0$ : it is near the low-mass end of the NSC mass-to-galaxy-mass (Figure 6), radius-to-mass (Figure 8, bottom left), and density-to-mass (Figure 8, bottom right) relations. Nonetheless, a canonical observational marker is the steepening of surface brightness profiles near the central region of a galaxy (e.g. Lambert et al. 2024). Accordingly, we fit the surface brightness of the entire galaxy after the formation of the NSC with a

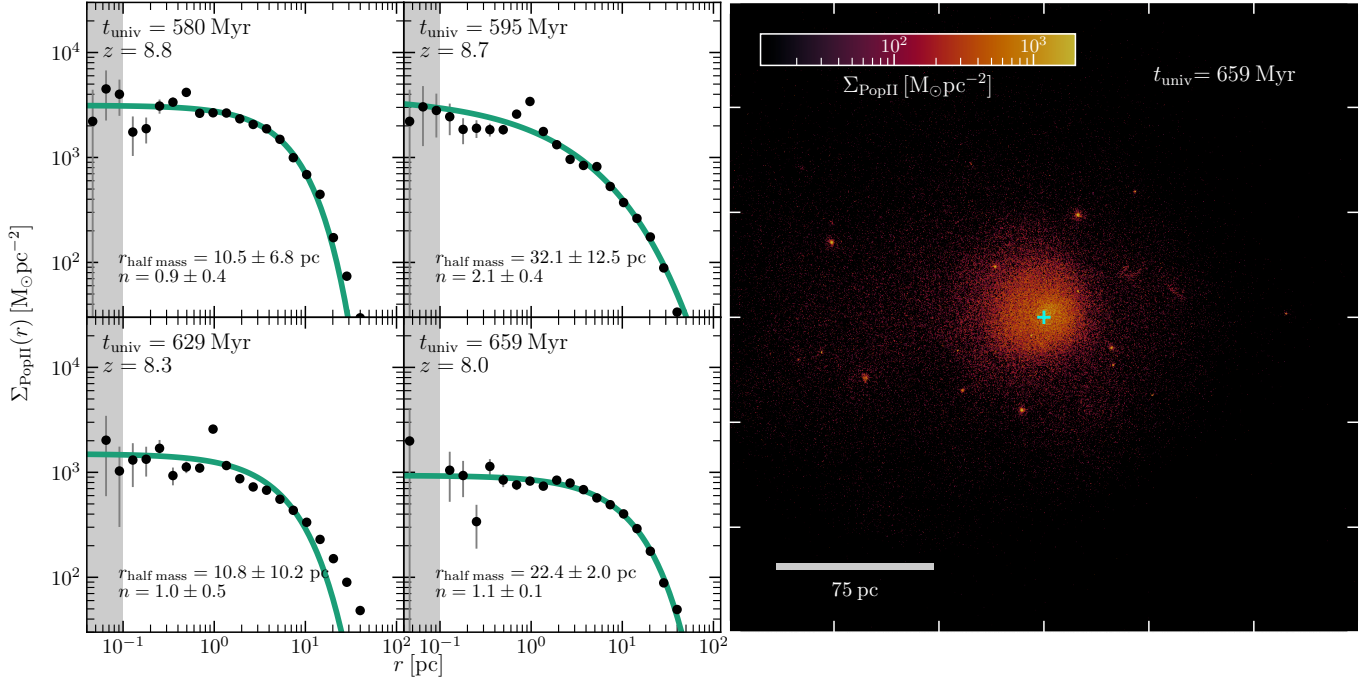


FIG. 10.— Evolution of the galaxy stellar surface density profiles  $\Sigma_{\text{PopII}}(r)$  after starburst (b) (left panels) fitted with a Sersic density profile (see text for details) centred on the NSC which is marked by a cyan crosshair in the projected stellar densities  $\Sigma_{\text{PopII}}$  shown on the right panel. The right panel corresponds to the bottom right surface density profile taken at  $z = 8.0$ . The errors depict Poisson noise.

Sersic profile (Sérsic 1963):

$$\mu_{\text{AB}}(r) = \mu_e + \frac{2.5b_n}{\ln(10)} \left[ \left( \frac{r}{r_{\text{half}}} \right)^{1/n} - 1 \right], \quad (3)$$

where  $r$  is the radial distance from the centre of the galaxy,  $\mu_e$  is the central brightness,  $n$  is the Sersic index,  $b_n = 1.9992n - 0.3721$  (Capaccioli 1989), and  $r_{\text{half}}$  is the characteristic radius encompassing half of the galaxy's total (in this case, UV) luminosity (Caon et al. 1993). Right after the NSC was formed, we see a slight steepening in the surface brightness near ( $\lesssim 3$  pc) the galaxy's centre. We quantify this in Figure 9 (bottom left) with a double-Sersic profile, which fits the NSC (with  $r_{\text{half}} = 8.7$  pc and  $n = 5.0$ ) and the host galaxy ( $r_{\text{half}} = 18.5$  pc and  $n = 2.0$ ) components separately.

Dashed and dotted circles in Figure 9 represent the characteristic radii of the NSC and galaxy components, respectively. The starburst drives the slight steepening in  $\mu_{\text{AB}}$  ( $\sim 2.5$  dex) as the bright, young stellar population and higher central densities amplify UV emission near the centre. UV surface brightness is highly variable due to stochastic star formation, causing the galaxy to dim significantly over  $\sim 10$  Myr (Figure 9, bottom right), making the NSC less distinguishable in radial UV profiles. By  $z = 8.0$ , stars formed offset the centre after starburst (b) dominate UV emission, slightly increasing the fitted half-light radius to  $r_{\text{half}} = 25.8$  pc (Figure 9, bottom right).

Given the variability in the galaxy's UV surface brightness, we also use a Sersic density profile:  $\Sigma(r) = \Sigma_0 \exp[-b_n(r/r_{\text{half mass}})^{1/n}]$  (Vital & Mamon 2020). Figure 10 (left panels) shows the evolution of the stellar surface density profiles for the entire galaxy,  $\Sigma_{\text{PopII}}(r)$ , after starburst (b) along with a non-linear least-squares fit.

The galaxy has a fluctuating half-mass radius  $r_{\text{half mass}} \approx 20 - 30$  pc, with a stable Sersic index of  $n \sim 1 - 2$ . Slight over-densities ( $\sim 3\times$  higher than the fit) near the centre ( $r \lesssim 1$  pc) are attributed to compact star clusters inspiralling toward the NSC. This is seen qualitatively in the stellar surface densities depicted in the right panel. At  $z = 8.8$ , right after the NSC was seeded, the central density reaches as much as a few  $10^3 \text{ M}_\odot \text{ pc}^{-2}$ . However, we see that the densities decrease slightly at  $z = 8.0$ , suggesting that the relatively low mass of the NSC and the dynamical heating of the broader galactic environment of the cluster prevent its core collapse (and subsequent formation of an inner cusp in the surface density profiles) (Merritt 2009). Note, however, that this may also be a resolution effect caused by the 0.15 pc gravitational softening in our simulations which may artificially prevent core collapse.

#### 2.4.1. Stellar populations in nuclear star clusters

We now examine the formation mechanism of the NSC by analyzing its stellar populations. Figure 11 (top left) shows that the NSC contains stars from all star-forming epochs, including  $\sim 300$  Myr-old stars predating the first starburst at  $t_{\text{univ}} \sim 360$  Myr. Looking at the cumulative distribution function (CDF), the NSC is partly made (around 40%) by stars formed in predominantly bound star clusters (masses ranging from a few  $100$  to  $10^5 \text{ M}_\odot$ ) during starburst (a) at  $z \sim 10$ . These first-generation star clusters underwent some tidal disruption and dissolution during a  $\sim 80$  Myr period of quiescence. A second starburst followed, with lower SFEs ( $\lesssim 35\%$ , see Figure 2), producing less bound clusters (Kroupa et al. 2001; Pfalzner & Kaczmarek 2013; Banerjee & Kroupa 2018). Afterwards, star formation proceeds in metal-enriched, highly-fragmented clouds, collectively contributing over

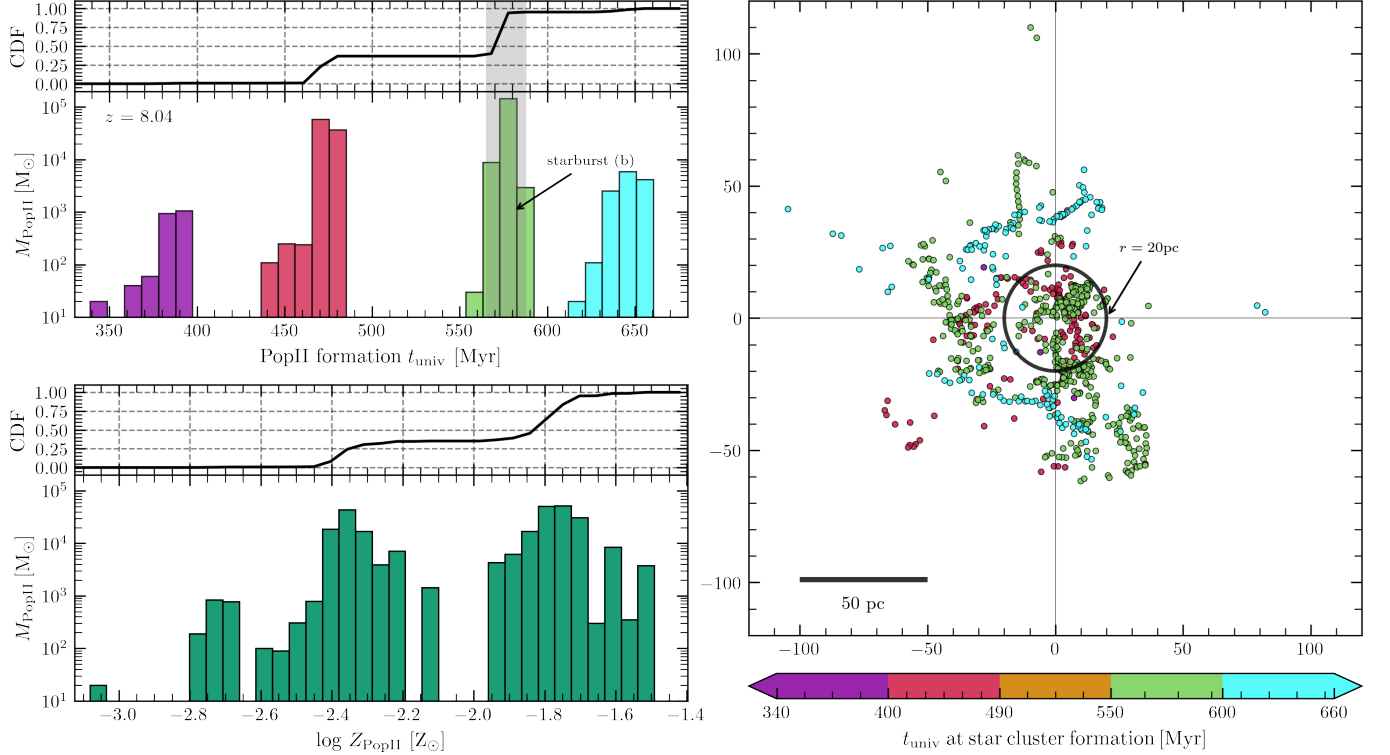


FIG. 11.— Stellar population that comprises the NSC. We show a mass distribution of Pop II stars ( $M_{\text{PopII}}$ ) comprising the NSC by the end of the simulation (top left), highlighting starburst (b) when the majority of the NSC mass was formed. Similarly, we also show the distribution of Pop II stellar mass per given metallicity bin in the NSC (bottom left). The right panel shows the positions of clouds identified in the simulation at the time they reach the critical density for star formation. We show their physical positions with respect to the centre of the galaxy (see text for the definition) and colour them based on their birth epoch (clouds that form stars during starburst (b) are coloured green). To guide the reader's eye, we indicate a circle with a radius of 20 pc which is  $\sim 2\times$  the typical half-mass radius of the NSC (refer back to Figure 10).

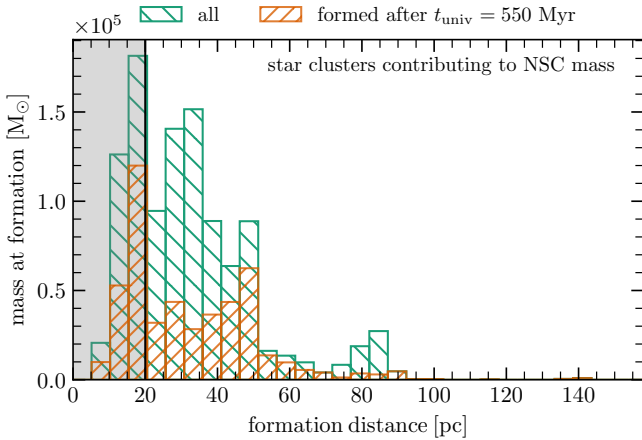


FIG. 12.— Distribution of formation distance from the centre of the galaxy/NSC for all star clusters (green) that have contributed at least a fraction of their stellar mass to the NSC. We show a subset of this distribution (orange) only for those formed at  $t_{\text{univ}} > 550$  Myr, during and after starburst (b). In situ NSC mass contribution is depicted by the orange distribution within the grey-shaded region, indicating star formation within  $< 20$  pc of the centre.

50% of the NSC mass by  $z = 8.0$ .

We see a similarly multi-peaked distribution looking at the stellar metallicities (Figure 11, bottom left), which contain star particles with metallicities as low as  $Z_{\text{PopII}} = 8 \times 10^{-4} Z_{\odot}$  and recently-formed stars of metallicity as

high as  $Z_{\text{PopII}} = 3 \times 10^{-2} Z_{\odot}$ . Moreover, we mention the minor detail that there is not a direct correspondence between the  $t_{\text{univ}}$  and  $Z_{\text{PopII}}$  distribution, a point we made earlier when looking at Figure 4. The NSC consists of stars from all star-forming periods; however, the CDF in the bottom left panel of Figure 11 shows that it is predominantly ( $> 50\%$ ) made of stars with  $Z_{\text{PopII}} > 10^{-2} Z_{\odot}$ .

The oldest constituent stars in the NSC are a couple of star particles from the first Pop II star cluster formed at  $z = 12.95$  ( $t_{\text{univ}} \sim 350$  Myr) with metallicities  $Z_{\text{PopII}} \sim 2 \times 10^{-4} Z_{\odot}$ . This large metallicity spread ( $-3.5 < \log(Z/Z_{\odot}) < -1.5$ ) of the NSC, when compared to those within individual star clusters shown in Figure 7, is further confirmation that the NSC is formed – for a large fraction of its mass – by accreting older star clusters.

#### 2.4.2. In situ star formation versus star cluster in-spiral

We examine the origin of the NSC further by looking at the sites of formation for all stars in the NSC, depicted in the right panel of Figure 11. This figure shows the physical positions of star-forming clouds w.r.t. the centre of the galaxy at the time the cloud reaches  $n_{\text{H,crit}}$ . Immediately, we see that all clouds that contributed mass to the NSC formed stars within 200 pc (physical) of the galaxy's centre. Since the virial radius ( $r_{\text{vir}}$ ) of this halo grows from around  $r_{\text{vir}} \sim 1.2 - 3.4$  kpc throughout the simulation, star formation occurs exclusively within  $0.1 r_{\text{vir}}$  from the halo centre. Furthermore,



the spatial distribution of the sites of cloud formation shows that star formation, especially at later times, is clustered in elongated structures resembling filaments or shells.

The circle in the right panel of Figure 11 encloses a central region with a radius of 20 pc, roughly two times the  $r_{\text{half mass}}$  of the NSC at  $z = 8.0$  (Figure 8). If we define star formation taking place within this region right before and after starburst (b) ( $t_{\text{univ}} > 550$  Myr) to be in-situ star formation, we conclude that while there is some in situ star formation that contributed to the growth of the NSC, the majority of the star clusters were formed ex-situ. To confirm this, Figure 12 shows the distribution of (3D) physical distances between the galaxy’s centre and the clouds’ position at the time of formation. This Figure shows the distances of the newly-formed star clusters from the centre, weighted by that cluster’s mass at formation. That is, not all stars from a star cluster necessarily become members of the NSC. Only  $\sim 20\%$  total by mass of the green distribution shown in Figure 12 have made it to the NSC. This fraction should sound familiar given that nearly all star-forming periods contributed to the growth of the NSC, which comprises around 20% of the galaxy’s total mass by  $z = 8$  (see Section 2.3.2). Regardless, a small fraction by mass – around 17% – of the NSC donor star clusters formed stars in situ (after 550 Myr and within 20 pc of the galaxy’s centre). This in situ fraction is shown as the shaded orange distribution in Figure 12.

In addition to the small NSC mass contribution from in situ star formation by  $z = 8.0$ , we also note that star formation post starburst (b) occurs almost exclusively just outside of the NSC (cyan points in Figure 11, right panel). This is likely due to feedback from the preceding starburst preventing the gas from reaching  $n_{\text{H,crit}}$  near the centre of the galaxy. The star-forming clouds are distributed in a ring-like structure that resembles a nuclear stellar ring (Comerón et al. 2010; Brandl et al. 2012; Ma et al. 2018). However, this structure is probably unstable dynamically, and a stellar ring will likely be short-lived.

The results above suggest that the formation of the NSC comes from two pathways: (i) old star clusters that eventually evaporated due to dynamical relaxation and/or disrupted due to external perturbations as they migrate inward to the centre of the galaxy and (ii) open star clusters that formed in-situ (within 20 pc) near the centre of the galaxy. At this stage of the galaxy’s evolution, the dominant pathway for NSC growth is via star cluster accretion and dissolution while in-situ star formation marginally contributes to the mass at merely 17%.

### 3. DISCUSSION AND CONCLUSIONS

To our knowledge, this is the first cosmological RHD simulation of a galaxy that forms both massive bound star clusters and a central object resembling an NSC at  $z \gtrsim 8.0$ . We discuss our results within the broader effort to study high-redshift bound star clusters, now being observed by JWST, and postulate potential links to NSC formation.

#### 3.1. Comparison to recent observations of magnified star clusters at high redshift

Here, we draw comparisons between the star clusters formed in our simulations and those recently observed

by the JWST aided by strong gravitational lensing. We refer to Figure 8 for relevant star cluster properties and scaling relationships in our simulation.

Vanzella et al. (2023) presented NIRCcam photometric observations of Sunrise Arc, a lensed galaxy at  $z_{\text{phot}} = 6.0 \pm 0.2$ . The entire galaxy has an estimated stellar mass of  $M_{\star} \sim 0.3 - 2.0 \times 10^9 M_{\odot}$  with roughly 10 to 30% of its mass locked in 6 detected star clusters with individual masses  $m_{\text{star cluster}} \sim 10^{6-7} M_{\odot}$ . These star clusters are young (ages  $\lesssim 5-30$  Myr), compact (effective half-light radii  $\sim 1-25$  pc), and have high stellar surface densities:  $\Sigma_{\star} \sim 1.5-12.0 \times 10^3 M_{\odot} \text{ pc}^{-2}$ , with one cluster in particular reaching up to a few  $10^6 M_{\odot} \text{ pc}^{-2}$ .

Another set of observations is of the Cosmic Gems Arc at an even higher redshift ( $z_{\text{phot}} \sim 10.2$ ) by Adamo et al. (2024b), revealing an even more extreme population of star clusters that – while having similar masses with 5 identified young star clusters (ages  $\sim 9-36$  Myr,  $m_{\text{star cluster}} \sim 10^6 M_{\odot}$ ) hosting 30% of the galaxy’s total mass of  $M_{\star} \sim 2.4 - 5.6 \times 10^7 M_{\odot}$  – have much lower estimated radii ( $\lesssim 1$  pc) and generally higher surface densities  $\Sigma_{\star} > 10^5 M_{\odot} \text{ pc}^{-2}$ .

Most recently, Mowla et al. (2024) reported spectroscopic observations of the Firefly Sparkler galaxy (Mowla et al. 2022). Confirmed at  $z_{\text{spec}} = 8.296 \pm 0.001$ , this galaxy has a stellar mass estimate of  $M_{\star} \sim 5.0 \times 10^6 - 1.0 \times 10^8 M_{\odot}$  and is made of up to 57% by mass from compact ( $\lesssim 4-7$  pc), young (ages  $\sim 2-8$  Myr assuming instantaneous SSP burst) star clusters with masses  $\sim 10^{5-6} M_{\odot}$  and densities  $\Sigma_{\star} \gtrsim 10^{3-4} M_{\odot} \text{ pc}^{-2}$ .

The relatively young star cluster population formed in our simulation (ages  $\lesssim 20$  Myr at  $z = 9.9$ ) bear most resemblance to those presented in Mowla et al. (2024), though they tend to be less massive ( $m_{\text{star cluster}} \lesssim 10^5 M_{\odot}$ , more compact ( $r_{\text{half mass}} \lesssim 3$  pc), and less dense ( $\Sigma_0 \lesssim 2 \times 10^4 M_{\odot} \text{ pc}^{-2}$ ) than the current observations. However, because the sources in Mowla et al. (2024) are unresolved, they are likely to be smaller and denser. We also highlight the fact that although our simulations have a sub-pc resolution ( $\Delta x_{\text{min}} = 0.15$  pc at  $z = 9$ ), higher resolution is likely required to not only resolve smaller star clusters but also to reliably track the dynamics and maintain the high densities of these parsec-sized objects.

The galaxy in this work reaches a maximum bound star cluster formation efficiency (CFE) of more than 60% during the formation of the first few star clusters at  $z \sim 11.6$ . The CFE decreases to nearly 50% during the first starburst at  $z \sim 10$  (around 75 Myr after) when the galaxy had a mass of  $M_{\star} = 8.4 \times 10^5 M_{\odot}$ . Figure 13 shows these mass fractions in addition to the mass in the NSC that forms near the end of the simulation. By redshift  $z = 8.29$ , the galaxy’s total mass is  $M_{\star} = 1.4 \times 10^6 M_{\odot}$  with a CFE of 25%. The CFE remains relatively stable at 20% near the end of the simulation at  $z \sim 8.0$ , with the NSC dominating much of the total mass of the bound systems in the galaxy, roughly 75 Myr after starburst (b) and 175 Myr after starburst (a). The variability in the measured CFE here is consistent with observations, which suggests CFEs ranging between 40 - 60 % (Vanzella et al. 2023; Adamo et al. 2024b; Mowla et al. 2024). The symbols in Figure 13 (bottom) compare our results with CFEs from JWST observations cent (Adamo et al. 2024b; Mowla et al. 2024). Given that we only have

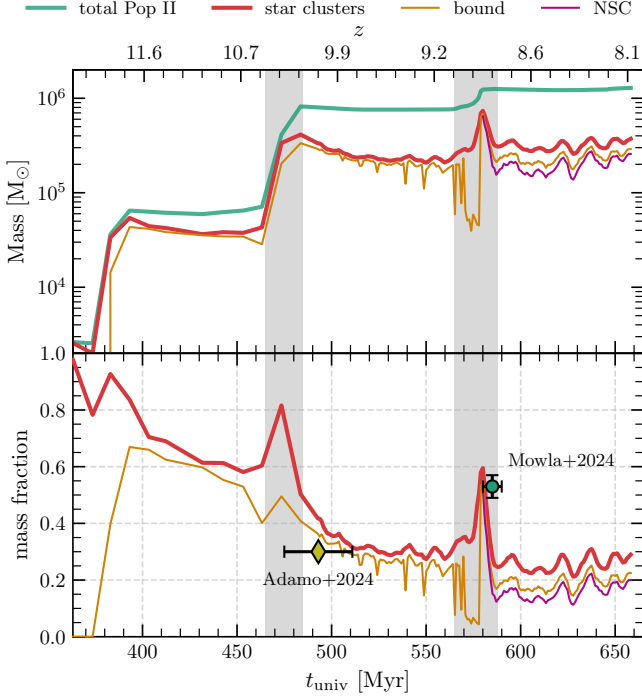


FIG. 13.— Star cluster formation efficiencies. In the top row, we show the total mass of Pop II stars similar to Figure 2 (note, the grey regions are also adopted from the same figure) in addition to the total mass residing in star clusters (both open and bound), bound star clusters, and the NSC after it was initially seeded during starburst (b). In the bottom row, we calculate the mass fraction of these quantities with the overall Pop II stellar mass of the galaxy (green line above), showing them with cluster formation efficiencies reported by (Adamo et al. 2024b) and (Mowla et al. 2024). Note that, for the observations (symbols), the depicted times have been slightly changed with respect to the observed redshifts such that the observed ages of the star clusters are correctly reproduced assuming they form during the the nearest starburst in our simulated galaxy.

one realization of a simulated galaxy, instead of placing the data points from the observations at the galaxies’ observed redshifts, we place them after the nearest starburst: burst (a) or (b). More specifically, we placed them at times such that the horizontal error bars have widths that encapsulate the range of star cluster ages (stated above), with the lower bounds corresponding to the peak of the nearest starburst. Given this caveat, the CFE predicted by the simulation is within the observed range and is consistent with both observed values.

It is important to note that the star clusters observed at  $z > 6$  by JWST are hosted in galaxies with halo masses greater than in our simulation, typically Milky Way progenitors or more massive galaxies (Mowla et al. 2024). Therefore, the maximum star cluster mass and the number of GC progenitors in our simulated galaxy is more typical of a lower-mass halo, consistent with the GC-to-halo mass ratios seen in observations (Forbes et al. 2018; Eadie et al. 2022; Jones et al. 2023) and theoretical predictions from cosmological hydrodynamic simulations (Doppel et al. 2022) suggesting that lower mass galaxies  $M_\star < 10^9 M_\odot$  have lower GC occupation fractions. Therefore, if the progenitors of present-day GCs are indeed formed at  $z > 6$ , they are more likely to form in a higher-mass galaxy than the one presented here.

### 3.2. Nuclear star cluster formation

The existence of a central NSC is a fairly common attribute in most galaxies. The nucleation fraction increases in more massive galaxies ( $> 90\%$  for galaxies with  $M_\star \sim 10^9 M_\odot$ ) (e.g., Sánchez-Janssen et al. 2019), and decreases in low mass galaxies  $\sim 10^6 M_\odot$  at  $z \sim 0$  (Carlsten et al. 2020; Neumayer et al. 2020). Studies as early as those by Tremaine et al. (1975) have proposed in-spiral of GCs due to dynamical friction as a natural formation mechanism for NSCs, with the most massive star clusters especially vulnerable to such fate (Neumayer et al. 2020). This scenario is well established, in part due to observations of metal-poor stars at the centre of dwarf galaxy NSCs (e.g., Alfaro-Cuello et al. 2020; Fahrion et al. 2020) that were proposed likely to be tidal remnants of these in-spiralling objects (Perets & Mastrobuono-Battisti 2014). Indeed, this scenario is likely the most common pathway for NSC growth for low mass ( $\lesssim 10^9 M_\odot$ ) galaxies presuming they contain a substantial population of star clusters with masses  $\gtrsim 10^5 M_\odot$  that can grow the NSC mass (Agarwal & Milosavljević 2011; Neumayer et al. 2011; Neumayer et al. 2020). However, the amount of mass contributed to the NSC via this process ultimately depends on the high-mass truncation of the ICMF, which in our case is roughly  $m_{\text{CMF, trunc}} \sim 10^5 M_\odot$ , with higher masses leading to more massive and extended NSCs that more comfortably fall within scaling relations (Agarwal & Milosavljević 2011).

Otherwise, in-situ star formation fueled by the infall of dense gas (Loose et al. 1982; Mihos & Hernquist 1994) near the centre of the galaxy is needed to reproduce kinematics and observed luminosity functions of NSC-hosting galaxies (Hartmann et al. 2011; Antonini et al. 2012). Predictions by semi-analytical models and simulations suggest that it is rather a combination of the two (Gnedin et al. 2014; Brown et al. 2018). For example, a *wet migration* scenario (as opposed to “dry” mergers and dissolution of GCs) in isolated dwarf galaxies presented in Guillard et al. (2016) posits that a YMC can form stars in a gas-rich disk and maintain a gas reservoir for star formation as it in-spirals to the nucleus of the galaxy. Most recently, a starburst-induced in-situ formation of an NSC has been explored in dwarf galaxies at  $z \sim 1.4 - 0$  by Gray et al. (2024). Furthermore, a hybrid NSC formation scenario is identified by van Donkelaar et al. (2024) using cosmological hydrodynamic simulations of a MW-mass galaxy at  $z > 4$  whereby an NSC can partly form (a maximum of 20% of its mass) from this mechanism. The rest of the NSC mass is supplied by both disc and bar-funnelled gas into the galactic centre (van Donkelaar et al. 2024).

We see a similar hybrid formation scenario in our simulation, albeit for a dwarf galaxy progenitor occurring at a much earlier time – within 1 Gyr of cosmic history – with the majority ( $\gtrsim 80\%$ ) of the mass coming from the infall and disruption of the first star clusters suggesting that this is the dominant mechanism during the initial phase of NSC seeding and growth. This work hints at a possible pathway for the transition between the clustered star formation we see at high- $z$  (Vanzella et al. 2023; Adamo et al. 2024b; Mowla et al. 2024) to the seeding of a centrally dominant NSC at redshifts as early as  $z \sim 8.0$ , about 700 Myr after the Big Bang.

#### 4. CONCLUSIONS

We present a high-resolution cosmological RHD zoom-in simulation of a typical mass galaxy evolving during the first 700 Myr of cosmic history (in a  $10^{8-9} M_{\odot}$  DM halo), with UV luminosity comparable to the faintest galaxies observed by JWST at similar redshifts. The work presented in this paper is the natural extension of our previous study (G23), focusing on how changing the star formation efficiencies in molecular clouds affects the formation and evolution of the first star clusters at redshifts  $z > 8$ . These simulations resolve (at  $\sim 0.15$  pc resolution) star cluster formation into individual massive ( $m_* = 10 M_{\odot}$ ) star particles that emit radiation and inject thermal feedback from CCSNe. In G23, we compared two models: the HSFE model with 70% efficiency and the LSFE model with 35% efficiency in star-forming clouds. In this study, we implement a more realistic sub-grid model (the VSFE model) where the SFEs in star-forming clouds vary depending on their densities, masses, and metallicities. He et al. (2019) derived the VSFE model we adopted in the present simulations using a grid of high-resolution (AU-scale) RMHD simulations of turbulent molecular clouds. Using this multi-scale approach, our study finds the following:

1. Using a realistic star formation model with cloud-dependent SFEs, a dwarf galaxy ( $M_* \sim 10^{10} M_{\odot}$  at  $z = 0$ ) progenitor produces, by  $z \sim 8$ , a population of small (0.1 - 3 pc) bound star clusters with masses reaching  $\sim 10^5 M_{\odot}$  (nearly  $10\times$  more massive than what was initially presented in G23). These star clusters have properties consistent with those discovered in JWST observations of strongly lensed galaxies at  $z > 6$ : they have stellar surface densities ranging between a few  $100 - 2 \times 10^4 M_{\odot} \text{ pc}^{-2}$  and are formed in dense ( $\Sigma_{\text{cloud}} \sim 2 \times 10^3 M_{\odot} \text{ pc}^{-2}$ ), metal-poor ( $Z_{\text{cloud}} \sim 10^{-3} Z_{\odot}$ ) star-forming clouds at redshifts  $z = 12.0 - 9.0$ . The SFEs in these clouds reach values as high as 80%.
2. Adopting a cloud-dependent SFE model also increases the total stellar mass in the galaxy and the stochasticity of star formation compared to the constant high (70%) and low (35%) SFE models. The galaxy with this model experiences the longest period of quiescence (80 Myr, as opposed to HSFE's 70 Myr), and the highest peaks of SFR, doubling the HSFE model's  $0.12 M_{\odot} \text{ yr}^{-1}$ .
3. Cloud's SFEs decrease over time due to higher metal enrichment which allows clouds to fragment and form less massive (a few 100 to  $10^3 M_{\odot}$ ) unbound/open star clusters, causing the star cluster mass function – well described by a power law:  $dN/d \log m_{\text{star cluster}} \propto m_{\text{star cluster}}^{\Gamma}$  – to gradually steepen from  $\Gamma = -0.3$  to  $\Gamma = -1.1$ , which is still much flatter than typical slopes observed at low-redshifts. The galaxy-scale bound cluster formation efficiency decreases over time with a maximum of 60% at  $z = 12.0$  to only 20% at  $z = 8.0$ .
4. We also find that each star cluster has a metallicity spread of 0.05 - 0.1 dex, roughly scaling with the cluster mass, due to inhomogeneities or gradients

in the gas metallicity of the natal environment (i.e., pre-enrichment inhomogeneities).

5. The star cluster system at  $z = 9.69$  is produced by the rapid fragmentation of infalling gas filaments that form stars before reaching the halo centre. Hence, the clusters orbit within 150 pc of the galaxy centre, which remains largely devoid of stars. However, at redshift  $z \sim 8.7$ , a nuclear star cluster (NSC) (mass of  $\sim 2 \times 10^5 M_{\odot}$  and half mass radius of 10 pc corresponding to a central density of  $10^3 M_{\odot} \text{ pc}^{-2}$ ) forms from the in-spiral and dynamical disruption of star clusters, with the majority of the total NSC mass (83%) coming from unbound clusters formed at lower ( $\lesssim 30\%$ ) SFEs. The formation of the central star cluster also influences the population of bound star clusters formed at high SFEs, causing them to migrate inwards and lose mass. A sub-dominant fraction of the NSC mass ( $\sim 17\%$ ) comes from in-situ star formation. Forming a compact NSC at such early cosmic times has interesting implications for SMBH seeding models and for interpreting the “little red dots” population recently discovered by JWST at  $z \gtrsim 5$ .

The results presented here come with several caveats and are likely to improve with more detailed astrophysical models; e.g., tracking metal yields from various sources and more thorough consideration of pre-SN feedback like stellar winds (Andersson et al. 2024). Furthermore, higher numerical fidelity is also crucial since even though we resolve scales as small as 0.15 pc, current observations suggest that the first star clusters are even more compact (Adamo et al. 2024b; Mowla et al. 2024). The Pop II stars are also represented rather simplistically, with each star particle being  $10 M_{\odot}$ . Our current targets for improvement include: (i) extending the sample of galaxies to include more massive halos, since everything presented thus far is based on the study of one dwarf galaxy analogue; (ii) a more accurate, star-by-star treatment of Pop II stars with masses sampled from an IMF; and (iii) increasing the fidelity of our Pop III star formation model to be consistently determined by cloud-scale properties (e.g., Hirano et al. 2015) which is crucial in setting the stage for the metallicity evolution of the first Pop II star clusters. We leave these aforementioned improvements for future work.

#### ACKNOWLEDGEMENTS

FABG acknowledges support from the U.S. Department of Energy, Office of Science, and Office of Advanced Scientific Computing Research, under Award Number DE-SC0025528. This research is also supported by Grants-in-Aid for Scientific Research (KS: 22KK0043, 24H00002) from the Japan Society for the Promotion of Science. The authors acknowledge the University of Maryland's supercomputing resources (hpcc.umd.edu).



## REFERENCES

- Adamo A., et al., 2020, *Space Science Reviews*, 216, 69
- Adamo A., et al., 2024a, *arXiv e-prints*, p. [arXiv:2405.21054](#)
- Adamo A., et al., 2024b, *Nature*, 632, 513
- Agarwal M., Milosavljević M., 2011, *ApJ*, 729, 35
- Akins H. B., et al., 2023, *ApJ*, 956, 61
- Alfaro-Cuello M., et al., 2020, *ApJ*, 892, 20
- Andersson E. P., Mac Low M.-M., Agertz O., Renaud F., Li H., 2024, *A&A*, 681, A28
- Antonini F., Capuzzo-Dolcetta R., Mastrobuono-Battisti A., Merritt D., 2012, *ApJ*, 750, 111
- Applebaum E., Brooks A. M., Quinn T. R., Christensen C. R., 2020, *MNRAS*, 492, 8
- Atek H., et al., 2024, *Nature*, 626, 975
- Baggen J. F. W., et al., 2024, *ApJ*, 977, L13
- Bailin J., 2018, *ApJ*, 863, 99
- Banerjee S., Kroupa P., 2018, in *Stahler S., ed., Astrophysics and Space Science Library* Vol. 424, The Birth of Star Clusters. p. 143 ([arXiv:1512.03074](#)), doi:10.1007/978-3-319-22801-3\_6
- Bastian N., Lardo C., 2018, *ARA&A*, 56, 83
- Bekki K., 2019, *A&A*, 622, A53
- Bellovary J., 2025, *arXiv e-prints*, p. [arXiv:2501.03309](#)
- Bondi H., 1952, *MNRAS*, 112, 195
- Boylan-Kolchin M., 2024, *arXiv e-prints*, p. [arXiv:2407.10900](#)
- Brandl B. R., Martín-Hernández N. L., Schaerer D., Rosenberg M., Werf P. P. v. d., 2012, *A&A*, 543, A61
- Bromm V., Yoshida N., 2011, *ARA&A*, 49, 373
- Brown G., Gnedin O. Y., Li H., 2018, *ApJ*, 864, 94
- Burkhart B., 2018, *ApJ*, 863, 118
- Calura F., et al., 2024, *arXiv e-prints*, p. [arXiv:2411.02502](#)
- Caon N., Capaccioli M., D'Onofrio M., 1993, *MNRAS*, 265, 1013
- Capaccioli M., 1989, in *Corwin Jr. H. G., Bottinelli L., eds., World of Galaxies (Le Monde des Galaxies)*, pp 208–227
- Carlsten S. G., Greco J. P., Beaton R. L., Greene J. E., 2020, *ApJ*, 891, 144
- Carlsten S. G., Greene J. E., Beaton R. L., Greco J. P., 2022, *ApJ*, 927, 44
- Charlie C., Spergel D. N., 2010, *ApJ*, 726, 36
- Chen Y., Gnedin O. Y., 2023, *MNRAS*, 522, 5638
- Chevanne M., et al., 2020, *Space Science Reviews*, 216, 50
- Comerón S., Knapen J. H., Beckman J. E., Laurikainen E., Salo H., Martínez-Valpuesta I., Buta R. J., 2010, *MNRAS*, 402, 2462
- Costa G., Mapelli M., Iorio G., Santoliquido F., Escobar G. J., Klessen R. S., Bressan A., 2023, *MNRAS*, 525, 2891
- Davies M. B., Miller M. C., Bellovary J. M., 2011, *ApJ*, 740, L42
- Doppel J. E., et al., 2022, *MNRAS*, 518, 2453
- Eadie G. M., Harris W. E., Springford A., 2022, *ApJ*, 926, 162
- Efstathiou G., Davis M., White S. D. M., Frenk C. S., 1985, *ApJS*, 57, 241
- El-Badry K., Quataert E., Weisz D. R., Choksi N., Boylan-Kolchin M., 2019, *MNRAS*, 482, 4528
- Fahrion K., et al., 2020, *A&A*, 634, A53
- Fahrion K., et al., 2021, *A&A*, 650, A137
- Fahrion K., et al., 2022, *A&A*, 667, A101
- Finkelstein S. L., et al., 2023, *ApJ*, 946, L13
- Forbes D. A., Read J. I., Gieles M., Collins M. L. M., 2018, *MNRAS*, 481, 5592
- Fujimoto S., et al., 2024, *arXiv e-prints*, p. [arXiv:2402.18543](#)
- Fukushima H., Yajima H., 2021, *MNRAS*, 506, 5512
- Gao Y., Li H., Zhang X., Su M., Ng S. C. Y., 2024, *MNRAS*, 527, 7731
- García F. A. B., Ricotti M., Sugimura K., Park J., 2023, *MNRAS*, 522, 2495
- Gardner J. P., et al., 2023, *PASP*, 135, 068001
- Gnedin O. Y., Ostriker J. P., Tremaine S., 2014, *ApJ*, 785, 71
- Gray E. I., et al., 2024, *arXiv e-prints*, p. [arXiv:2405.19286](#)
- Greene J. E., et al., 2024, *ApJ*, 964, 39
- Grudić M. Y., Guszejnov D., Offner S. S. R., Rosen A. L., Raju A. N., Faucher-Giguère C.-A., Hopkins P. F., 2022, *MNRAS*, 512, 216
- Guillard N., Elmsselmen E., Renaud F., 2016, *MNRAS*, 461, 3620
- Hahn O., Abel T., 2011, *MNRAS*, 415, 2101
- Hartmann M., Debattista V. P., Seth A., Cappellari M., Quinn T. R., 2011, *MNRAS*, 418, 2697
- He C.-C., Ricotti M., Geen S., 2019, *MNRAS*, 489, 1880
- He C.-C., Ricotti M., Geen S., 2020, *MNRAS*, 492, 4858
- Hirano S., Hosokawa T., Yoshida N., Omukai K., Yorke H. W., 2015, *MNRAS*, 448, 568
- Inayoshi K., Visbal E., Haiman Z., 2020, *ARA&A*, 58, 27
- Jeon M., Ko M., 2024, *arXiv e-prints*, p. [arXiv:2411.17862](#)
- Jones M. G., et al., 2023, *ApJ*, 942, L5
- Katz H., Ricotti M., 2013, *MNRAS*, 432, 3250
- Katz H., Sijacki D., Haehnelt M. G., 2015, *MNRAS*, 451, 2352
- Katz H., Kimm T., Sijacki D., Haehnelt M. G., 2017, *MNRAS*, 468, 4831
- Kauffmann J., Pillai T., Goldsmith P. F., 2013, *ApJ*, 779, 185
- Kimm T., Katz H., Haehnelt M., Rosdahl J., Devriendt J., Slyz A., 2017, *MNRAS*, p. [stx052](#)
- King I., 1962, *The Astronomical Journal*, 67, 471
- Klessen R. S., Glover S. C. O., 2023, *ARA&A*, 61, 65
- Kokorev V., et al., 2024a, *arXiv e-prints*, p. [arXiv:2411.13640](#)
- Kokorev V., et al., 2024b, *ApJ*, 968, 38
- Kravtsov A., Belokurov V., 2024, *arXiv e-prints*, p. [arXiv:2405.04578](#)
- Kritos K., Beckmann R. S., Silk J., Berti E., Yi S., Volonteri M., Dubois Y., Devriendt J., 2024, Supermassive black hole growth in hierarchically merging nuclear star clusters, doi:10.48550/arXiv.2412.15334, [http://arxiv.org/abs/2412.15334](#)
- Kroupa P., Aarseth S., Hurley J., 2001, *MNRAS*, 321, 699
- Kruijssen J. M. D., 2015, *MNRAS*, 454, 1658
- Kruijssen J. M. D., Maschberger T., Moeckel N., Clarke C. J., Bastian N., Bonnell I. A., 2012, *MNRAS*, 419, 841
- Lambert M., Khim D. J., Zaritsky D., Donnerstein R., 2024, *The Astronomical Journal*, 167, 61
- Latour M., Kamann S., Martocchia S., Husser T. O., Saracino S., Dreizler S., 2025, *arXiv e-prints*, p. [arXiv:2501.09558](#)
- Leitherer C., et al., 1999, *ApJS*, 123, 3
- Loose H. H., Kruegel E., Tutukov A., 1982, *Astronomy and Astrophysics*, 105, 342
- Ma C., de Grijs R., Ho L. C., 2018, *ApJ*, 857, 116
- Ma X., Quataert E., Wetzel A., Faucher-Giguère C.-A., Boylan-Kolchin M., 2021, *MNRAS*, 504, 4062
- Matthee J., et al., 2024, *ApJ*, 963, 129
- McKenzie M., Bekki K., 2021, *MNRAS*, 507, 834
- Menon S. H., Lancaster L., Burkhardt B., Somerville R. S., Dekel A., Krumholz M. R., 2024, *ApJ*, 967, L28
- Merritt D., 2009, *ApJ*, 694, 959
- Mihos J. C., Hernquist L., 1994, *ApJ*, 437, L47
- Mondal A., Chattopadhyay T., 2024, *New Astronomy*, 108, 102182
- Mowla L., et al., 2022, *ApJ*, 937, L35
- Mowla L., et al., 2024, *Nature*, 636, 332
- Neumayer N., Walcher C. J., Andersen D., Sánchez S. F., Böker T., Rix H.-W., 2011, *MNRAS*, 413, 1875
- Neumayer N., Seth A., Böker T., 2020, *A&A Rev.*, 28, 4
- Oh S. P., Haiman Z., 2002, *ApJ*, 569, 558
- Pallottini A., Ferrara A., 2023, *A&A*, 677, L4
- Park J., Ricotti M., Sugimura K., 2021a, *MNRAS*, 508, 6176
- Park J., Ricotti M., Sugimura K., 2021b, *MNRAS*, 508, 6193
- Park J., Ricotti M., Sugimura K., 2023, *MNRAS*, 521, 5334
- Park J., Ricotti M., Sugimura K., 2024, *MNRAS*, 528, 6895
- Perets H. B., Mastrobuono-Battisti A., 2014, *ApJ*, 784, L44
- Pfalzner S., Kaczmarek T., 2013, *A&A*, 559, A38
- Pfeffer J., et al., 2024, *MNRAS*, 536, 1878
- Polak B., et al., 2024, *A&A*, 690, A94
- Renzini A., 2017, *MNRAS*, 469, L63
- Ricotti M., 2002, *MNRAS*, 336, L33
- Roberti L., Pignatari M., Fryer C., Lugaro M., 2024, *A&A*, 686, L8
- Rodríguez C. L., Hafen Z., Grudić M. Y., Lamberts A., Sharma K., Faucher-Giguère C.-A., Wetzel A., 2023, *MNRAS*, 521, 124
- Rosdahl J., Blaizot J., Aubert D., Stranex T., Teyssier R., 2013, *MNRAS*, 436, 2188
- Salpeter E. E., 1955, *ApJ*, 121, 161
- Sánchez-Janssen R., et al., 2019, *ApJ*, 878, 18
- Schaerer D., 2002, *A&A*, 382, 28
- Setton D. J., et al., 2024, *arXiv e-prints*, p. [arXiv:2411.03424](#)
- Shapiro K. L., Genzel R., Förster Schreiber N. M., 2010, *MNRAS*, 403, L36
- Spitzer L., 1987, *Dynamical evolution of globular clusters*, Princeton University Press
- Stiavelli M., et al., 2024, *arXiv e-prints*, p. [arXiv:2412.06517](#)
- Sugimura K., Matsumoto T., Hosokawa T., Hirano S., Omukai K., 2020, *ApJ*, 892, L14
- Sugimura K., Matsumoto T., Hosokawa T., Hirano S., Omukai K., 2023, *ApJ*, 959, 17
- Sugimura K., Ricotti M., Park J., García F. A. B., Yajima H., 2024, *ApJ*, 970, 14
- Sullivan J., Haiman Z., Kulkarni M., Visbal E., 2025, *arXiv e-prints*, p. [arXiv:2501.12986](#)
- Sérsic J. L., 1963, *Boletín de la Asociación Argentina de Astronomía La Plata Argentina*, 6, 41
- Teyssier R., 2002, *A&A*, 385, 337
- Tremaine S. D., Ostriker J. P., Spitzer Jr. L., 1975, *ApJ*, 196, 407
- Vanzella E., et al., 2023, *ApJ*, 945, 53
- Vázquez-Semadeni E., González-Samaniego A., Colín P., 2017, *MNRAS*, 467, 1313
- Vikaeus A., et al., 2024, *MNRAS*, 529, 1299
- Vital E., Mamon G. A., 2020, *A&A*, 635, A20

Wise J. H., Turk M. J., Norman M. L., Abel T., 2011, [ApJ](#), 745, 50  
Wise J. H., Regan J. A., O’Shea B. W., Norman M. L., Downes T. P., Xu H., 2019, [Nature](#), 566, 85  
Woosley S. E., Weaver T. A., 1995, [ApJS](#), 101, 181

Yajima H., Nagamine K., Zhu Q., Khochfar S., Dalla Vecchia C., 2017, [ApJ](#), 846, 30  
van Dokelaar F., Mayer L., Capelo P. R., Tamfal T., Quinn T. R., Madau P., 2023, [MNRAS](#), 522, 1726  
van Dokelaar F., Mayer L., Capelo P. R., Tamfal T., Quinn T. R., Madau P., 2024, [MNRAS](#), 529, 4104

This paper was built using the Open Journal of Astrophysics L<sup>A</sup>T<sub>E</sub>X template. The OJA is a journal which

provides fast and easy peer review for new papers in the **astro-ph** section of the arXiv, making the reviewing process simpler for authors and referees alike. Learn more at <http://astro.theoj.org>.